ACS Partner Journal

CHEMICAL & BIOMEDICAL IMAGING

pubs.acs.org/ChemBioImaging

Review

Enzyme-Instructed CBT-Cys-like Click Cyclization Reactions for Bioimaging

Yang Yang,[†] Xiaoyang Liu,[†] Xiaofeng Wu,* and Gaolin Liang*

Cite This: *Chem. Biomed. Imaging* 2024, 2, 98−116

Read Online

ACCESS | Metrics & More | Article Recommendations

ABSTRACT: With high efficiency, mild conditions, and rapid reaction rate, click reactions have garnered much attention in the field of bioimaging since proposed by Sharpless et al. in 2001 (*Angew. Chem., Int. Ed.* **2001**, *40*, 2004−2021). Inspired by the regenerative pathway of D-luciferin in fireflies, Liang et al. (*Nat. Chem.* **2010**, *2*, 54−60) raised a 2-cyanobenzothiazole (CBT)-cysteine (Cys) click condensation reaction in 2010, which exhibits a higher second-order reaction rate (9.19 M^{-1} s^{-1}) and superior biocompatibility. As it has been developed in the past decade, remarkable progress has been made in the construction of enzyme-instructed CBT-Cys-based bioimaging probes. This review introduces the concept of the CBT-Cys click reaction, elucidates the mechanism of the CBT-Cys click reaction, and concerns the development progress of CBT-Cys reaction and its derived reactions [i.e., 2-cyano-6-hydroxyquinoline (CHQ)-Cys reaction and 2-pyrimidinecarbonitrile (PMN)-Cys reaction]. Furthermore, we give a comprehensive and up-to-date review of enzyme-instructed CBT-Cys-like click reaction-based probes with significantly enhanced imaging signal and contrast for various bioimaging modes, including fluorescence imaging, photoacoustic imaging, magnetic resonance imaging, and positron emission tomography. In the end, we discuss the possible challenges and opportunities that may arise in the future.

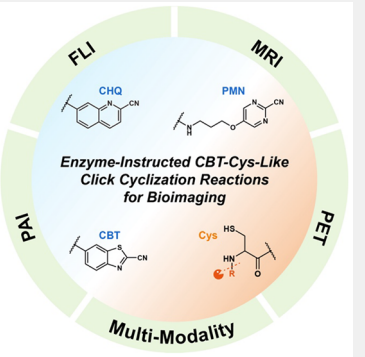

KEYWORDS: *Bioimaging, CBT-Cys-like reactions, Click chemistry, Cyclization reaction, Enzyme-instructed assembly*

1. INTRODUCTION

Molecular imaging has became a powerful technique, which is based on specific molecular probes and intrinsic tissue features as the sources of images, to monitor biological processes at the molecular and cellular levels within living organisms.[1,2] It enables noninvasive visualization and has been extensively applied in biomedical research and clinical disease diagnostics (especially for early diagnosis of tumor).[3] The imaging quality of molecular imaging largely relies on molecular probes. Therefore, it is essential to construct molecular probes possessing high sensitivity, high specificity, stability, and good biocompatibility.[4] Moreover, the complex microenvironments inside living organisms often challenge the selectivity and reaction rate of probes. Hence, compared with other types of reactions, click reactions with high selectivity and reaction efficiency may take advantages and further show great potential in the field of biomedical imaging.[5−7]

Click chemistry with high efficiency, mild conditions, and rapid reaction rate, was first raised by Sharpless et al. in 2001.[8] Among various click reactions, the copper-catalyzed azide−alkyne cycloaddition (CuAAC) reaction shows tremendous value in chemical synthesis without extra protecting groups and product purification.[9] However, copper(I) as a biounfriendly catalyst may induce potential biotoxicity, which limits the further biological applications of CuAAC reaction.[10,11] In order to reduce the toxicity in this copper-catalyzed reaction, Bertozzi et al. developed this reaction and devised a copper-free variant of click reaction by using substituted cyclooctyne with strain and electron-withdrawing ability to promote the [3 + 2] dipolar cycloaddition, thereby enhancing biocompatibility.[12] Further, Liang et al. were inspired by the regenerative pathway of D-luciferin in fireflies and developed a rapid and safe click condensation reaction between 2-cyanobenzothiazole (CBT) and cysteine (Cys) in 2010.[13] This reaction was named CBT-Cys reaction and features a rapid and specific formation of predominant cyclic dimers and a lesser extent of cyclic oligomers by incorporating CBT with *N*-terminal Cys in small molecules.[14] Then, in 2011, Ye et al. used 2-cyano-6-hydroxyquinoline (CHQ) to replace the CBT motif to overcome the interference from endogenous Cys encountered in CBT-Cys reactions.[15] Both of these two click reactions can be easily activated by relevant stimuli within the body (e.g., pH, reduction, or enzymes). Among these stimuli, enzymes as ubiquitous active substances in organisms and play pivotal roles in numerous physiological and pathological pro-

Received: October 31, 2023
Revised: December 4, 2023
Accepted: December 6, 2023
Published: December 31, 2023

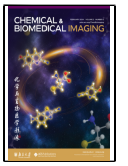

https://doi.org/10.1021/cbmi.3c00117
Chem. Biomed. Imaging 2024, 2, 98−116

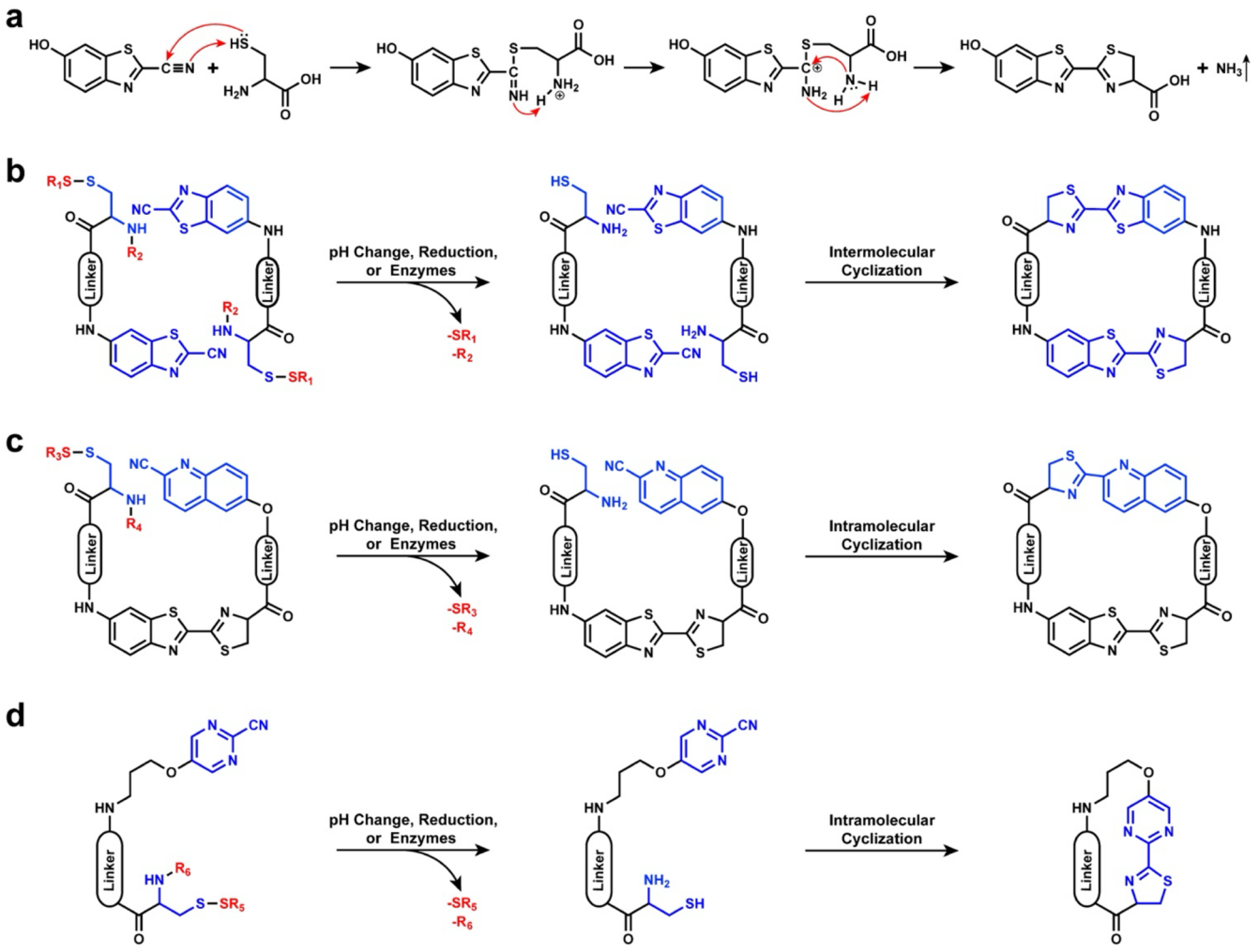

Figure 1. Reaction mechanism and cyclization routes of CBT-Cys-like click reactions. (a) Reaction mechanism of CBT-Cys click reaction. Classical stimuli-induced cyclization routes of CBT-Cys (b), CHQ-Cys (c), and 2-pyrimidinecarbonitrile (PMN)-Cys (d) reactions. Usually, SR_1, SR_3, and SR_5 represent the groups that are sensitive to reducing substances, and R_2, R_4, and R_6 are peptide sequences that can be specifically cleaved by enzymes.

cesses.[16,17] Extensive research has consistently demonstrated a direct correlation between aberrant enzyme expression and various diseases, thereby establishing that enzymes as widely acknowledged crucial biomarkers for multiple ailments may contribute to more precise molecular imaging.[18] Harnessing the potential of enzymes facilitates the development of "smart" probes, which can offer enhanced imaging contrast compared with conventional probes and thereby realize more accurate disease diagnoses.[19]

In recent years, CBT-Cys-like click cyclization reactions have been widely utilized to synthesize functional probes for catering to the molecular imaging requirements of higher specificity and contrast. Combined with different kinds of enzymes and their various expressions in pathological areas, enzyme-instructed CBT-Cys-like click reaction-constructed probes can be selectively activated at specific locations, thereby enabling more precise and distinct molecular imaging. Simultaneously, enzyme-instructed CBT-Cys-like click cyclization reactions can be applied to control the aggregation statement of probes that *in situ* assemble or disassemble in the abnormal locations by corresponding enzymes, thus enhancing the contrast between diseased areas and normal tissues. Consequently, the design and synthesis of bioimaging probes employing enzyme-instructed CBT-Cys-like click reactions hold immense significance for real-time disease monitoring and diagnosis. Herein, we introduce the concept and reaction mechanism of enzyme-instructed CBT-Cys-like click cyclization reactions and list their latest bioimaging applications for various imaging modalities, including fluorescence imaging (FLI), photoacoustic imaging (PAI), magnetic resonance imaging (MRI), and positron emission tomography (PET).[20−24] Furthermore, we also discuss the potential challenges and opportunities that may arise for these reactions in the future. It is anticipated that this review will inspire more designs of enzyme-instructed CBT-Cys-like click cyclization reaction probes for enhanced bioimaging.

2. MECHANISM OF THE CBT-CYS-LIKE CLICK REACTIONS

The CBT-Cys click reaction, as an important D-luciferin synthesis step in fireflies, owns great biosafety and a remarkable second-order reaction rate of 9.19 M^{-1} s^{-1}. The mechanism of CBT-Cys click reaction was clarified by Liang's group[25] and is depicted in Figure 1a. Under physiological pH conditions, the carbon atom on the cyano group of the CBT molecule

https://doi.org/10.1021/cbmi.3c00117
Chem. Biomed. Imaging 2024, 2, 98−116

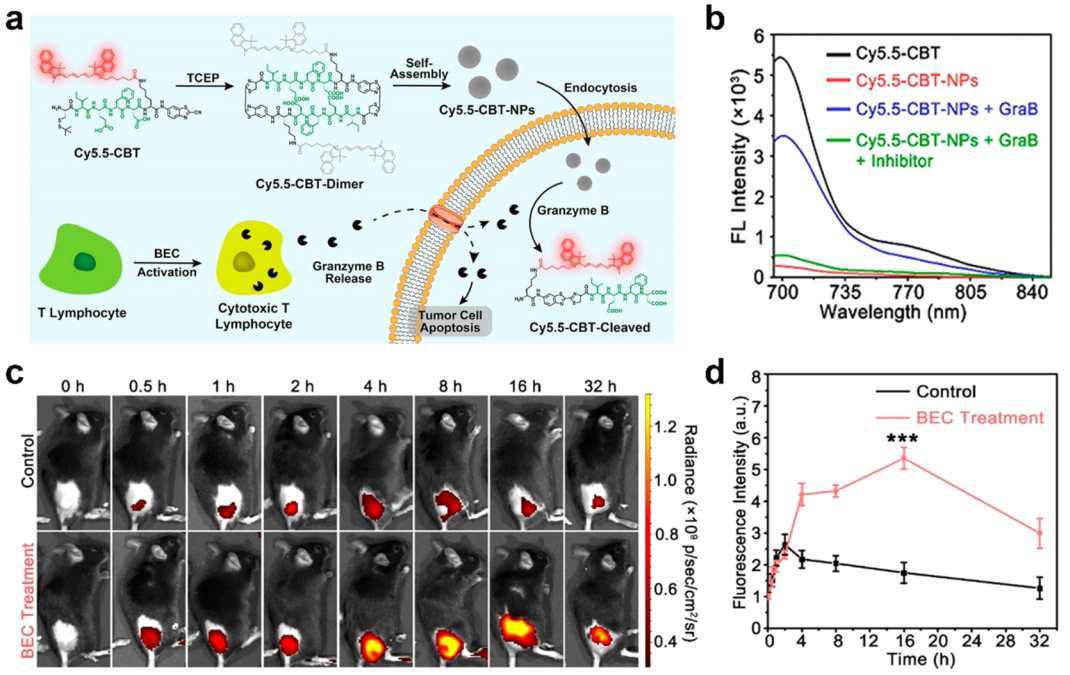

Figure 2. (a) Schematic illustration of FL-"dual-quenched" **Cy5.5-CBT-NPs** preparation and cartoon representation of using **Cy5.5-CBT-NPs** to image the tumoricidal activity of cytotoxic T lymphocytes. (b) FL spectra of **Cy5.5-CBT** (10 μM, black), **Cy5.5-CBT-NPs** (5 μM, red), and **Cy5.5-CBT-NPs** (5 μM) treated with 20 pM GraB (blue) or 20 pM GraB + 100 μM GraB inhibitor (green) in tris(hydroxymethyl)aminomethane (Tris, 100 mM, pH 7.5) buffer for 4 h, λ_{ex} = 675 nm, λ_{em} = 702 nm. (c) *In vivo* real-time FLI of B16-OVA tumor-bearing mice pretreated with saline (Control) or BEC (BEC treatment) for 3 days followed by intratumoral injection of 0.78 mg kg^{-1} **Cy5.5-CBT-NPs**. (d) Quantification of FL signals in (c). ***P < 0.001. Reproduced with permission from ref 41. Copyright 2022 American Chemical Society.

undergoes nucleophilic attack by the sulfur atom on the Cys, which results in a negatively charged nitrogen atom on the cyano group that captures a proton from the thiol group on the Cys and further leads to the formation of an intermediate with an enamine structure. Subsequently, the nitrogen atom on the formed enamine accepts a proton from the amino group on the Cys, followed by the simultaneous attack of positively charged carbon by nitrogen atoms on the amino groups of Cys while acquiring a third hydrogen atom from the cyano group's nitrogen atom. Consequently, this process generates ammonia (NH_3) as a product that is released into solution.[25] This reaction can be triggered by stimuli, such as pH, reduction, or enzymes, and shows great potential in biomedical applications by various controllable cyclization numbers of monomer molecules. The most common cyclic product of CBT-Cys reaction is cyclic dimers by intermolecular cyclization with occasional cyclic monomers (Figure 1b) when the linker is flexible. Conversely, when employing rigid scaffolds (i.e., glucose and cellulose carbohydrates), monomers readily assemble into linear polymers.[26,27]

In 2011, Ye and co-workers made notable progress in improving the CBT-Cys click cyclization reaction to address the issue of undesired side reactions caused by the abundance of endogenous free Cys in organisms.[15] Through a rigorous screening process involving multiple cyanide-substituted aromatic compounds, they successfully identified a promising CBT analogue known as CHQ, which exhibited an impressive reduction in reactivity toward free Cys more than 480-fold compared with CBT. As shown in Figure 1c, the reaction process between CHQ and Cys is similar to the CBT-Cys click reaction. Normally, by strategically manipulating the distance between CHQ and Cys, intramolecular cyclization can be induced within the noncyclic precursor, thereby leading to the formation of cyclic products with varying sizes. Moreover, the experiment results have proven that the CHQ-Cys cyclization reaction between noncyclic precursors and endogenous free Cys displayed less than 1% efficiency in cellular environments.

Additionally, Rao's group noticed the reaction difference between the CBT-Cys and CHQ-Cys and concluded that the reactivity of aromatic nitriles is influenced by the electron density of π-orbitals and the number of substituents in an aromatic ring.[28] Alkoxyl-substituted 2-pyrimidinecarbonitrile (PMN) was selected for facilitating biocompatible intramolecular cyclization click reactions (Figure 1d). Because of the lower second-order reaction rate of 0.01 M^{-1} s^{-1} with L-Cys, this PMN-Cys reaction can greatly eliminate the interference of free Cys. Therefore, the cyano group on aromatic structures can also react with Cys, and similar products are obtained. This exciting discovery expands the application range of CBT-Cys-like reactions. Importantly, the PMN-Cys reaction promotes the CBT-Cys-like reaction to bioorthogonal chemistry.

The class of CBT-Cys-like click reactions can address the challenge of macrocyclic compound generation from noncyclic precursors *in vivo* triggered by enzymes in the body. The formed macrocycles with favorable solubility, lipophilicity, metabolic stability, and bioavailability can further self-assemble into diverse nanostructures for expanding biomedical imaging applications.[29]

https://doi.org/10.1021/cbmi.3c00117
Chem. Biomed. Imaging 2024, 2, 98−116

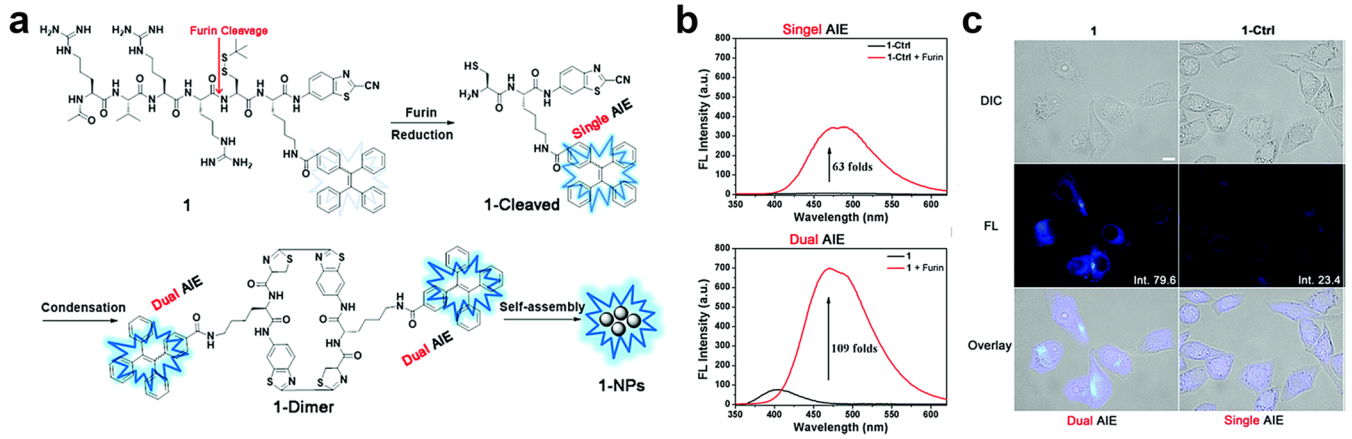

Figure 3. (a) Schematic illustration of furin-controlled dual aggregation-induced emission for enhanced FL sensing of furin activity. (b) Fluorescence spectra of 100 μM **1-Ctrl** (black) and 100 μM **1-Ctrl** incubated with 1 nmol U^{-1} furin at 37 °C for 4 h in furin buffer (red), respectively (top row). Fluorescence spectra of 100 μM **1** (black) and 100 μM **1** incubated with 1 nmol U^{-1} furin at 37 °C for 4 h in furin buffer (red) (bottom row). Excitation wavelength: 320 nm. (c) Differential interference contrast images (top row), fluorescence images (middle row, DAPI channel), and merged images (bottom row) of MDA-MB-468 cells incubated with 5 μM **1** (left column) or **1-Ctrl** (right column) coincubated with 50 μM Ac-Arg-Val-Arg-Arg-Cys(StBu)-Lys-CBT in a serum-free medium for 60 min at 37 °C and washed with PBS for three times prior to imaging, respectively. All images have the same scale bar: 10 μm. Reproduced with permission from ref 48. Copyright 2017 Royal Society of Chemistry.

3. BIOIMAGING APPLICATIONS OF ENZYME-INSTRUCTED CBT-CYS-LIKE CLICK CYCLIZATION REACTIONS

3.1. Fluorescence Imaging (FLI)

FLI as one of the most common bioimaging approaches mainly depends on fluorescent dyes capable of absorbing external excitation light energy and further emitting FL signals in the excited state.[30] FLI technique has gained widespread applications in disease diagnosis because of its exceptional spatiotemporal resolution and noninvasive characteristic.[31,32] With the rapid advancement of technology, conventional "always-on" FL probes with weak specificity and contrast have been replaced by smart "off-on" FL probes. These intelligent counterparts show the FL "off" state and, once entering the disease location, they can be cleaved by corresponding enzymes and turn into the FL "on" state.[33] This smart design imparts enhanced contrast and heightened sensitivity during the detection processes, thereby elevating their performances in bioimaging.

CBT-Cys-like click cyclization reactions can be easily conjugated with certain FL moieties to construct smart "off-on" FL probes. Cyclized CBT-Cys-like molecules always own strong hydrophobicity and show a tendency to aggregate into nanostructures. On the basis of this feature, some FL phenomenons [i.e., fluorescence resonance energy transfer (FRET) and aggregation-caused quenching (ACQ)] can be applied to construct CBT-Cys-like FL probes for achieving smart "off-on" bioimaging.[34−36] Du et al. designed a biotin-cystamine-Cys-Lys(cypate)-CBT molecule and successfully confirmed that the cypate on the CBT-Cys-dimer can achieve FRET effect.[37] The FL of cypate could turn off through intra- and intermolecular quenching, and thus, the formed nanoparticles can be used for enhanced photothermal therapy. For traditional organic fluorophores composed of planar and polycyclic π-conjugated frameworks, ACQ describes that they exhibit FL quenching in high-concentration solution or aggregation state but show high-efficiency luminescence in dilute solution.[38,39] Recent studies found the effectiveness of dual-quenched FL probes in significantly reducing background signals, thereby achieving enhanced detection sensitivity.[40] Xu et al. utilized the CBT-Cys click reaction to fabricate a dual-quenched FL probe, Cys(StBu)-Ile-Glu-Phe-Asp-Lys(Cy5.5)-CBT termed **Cy5.5-CBT**, for specific detection of granzyme B (GraB) activity and for monitoring the immunotherapy effect of cancer *in vivo*.[41] As shown in Figure 2a, *in vitro* reduction of disulfide bonds initially resulted in cyclic dimeric products via the CBT-Cys click reaction, which led to a single-quenched effect. Subsequently, intermolecular hydrophobic interactions and $\pi-\pi$ stacking facilitated spontaneous self-assembly into **Cy5.5-CBT-NPs** (NPs, nanoparticles) with "dual-quenched" FL signals. When being internalized by tumor cells, the probe underwent the cleavage of the Ile-Glu-Phe-Asp sequence by GraB, which resulted in nanoparticle disassembly and FL activation for the specific detection of GraB activity. The *in vitro* FL spectra result in Figure 2b proves that **Cy5.5-CBT-NPs** kept the lowest FL intensity and contributed to excellent dual quenching. Meanwhile, with the GraB addition, the FL could be quickly recovered. Furthermore, the *in vivo* real-time FL imaging results and their quantification of FL signals are shown in Figure 2c,d. The FL signals reached the maximum at 16 h in the immuno-activated B16-OVA tumor-bearing black mice by *S*-(2-boronoethyl)-L-cysteine hydrochloride (BEC) injection, and the intensity was 3-fold higher than that of the control group. By employing a dual-quenched strategy involving *in vitro* CBT-Cys cyclization and self-assembly, that study successfully developed dual-quenched probes that facilitate highly sensitive and specific imaging of intracellular expression levels of GraB and tumor-killing activity of cytotoxic T lymphocytes. These findings hold significant potential for the construction of dual-quenched Cys-CBT FL probes processing enzyme-instructed disassembly ability.

To avoid the influence induced by ACQ, Tang and co-workers introduced the concept of the aggregation-induced emission (AIE) effect in 2001.[42] Briefly, in diluted solutions, specific functional groups within AIE molecules undergo intramolecular rotation, which nonradiatively annihilates its excited state and renders its molecule nonluminescent,[43] while

https://doi.org/10.1021/cbmi.3c00117
Chem. Biomed. Imaging 2024, 2, 98−116

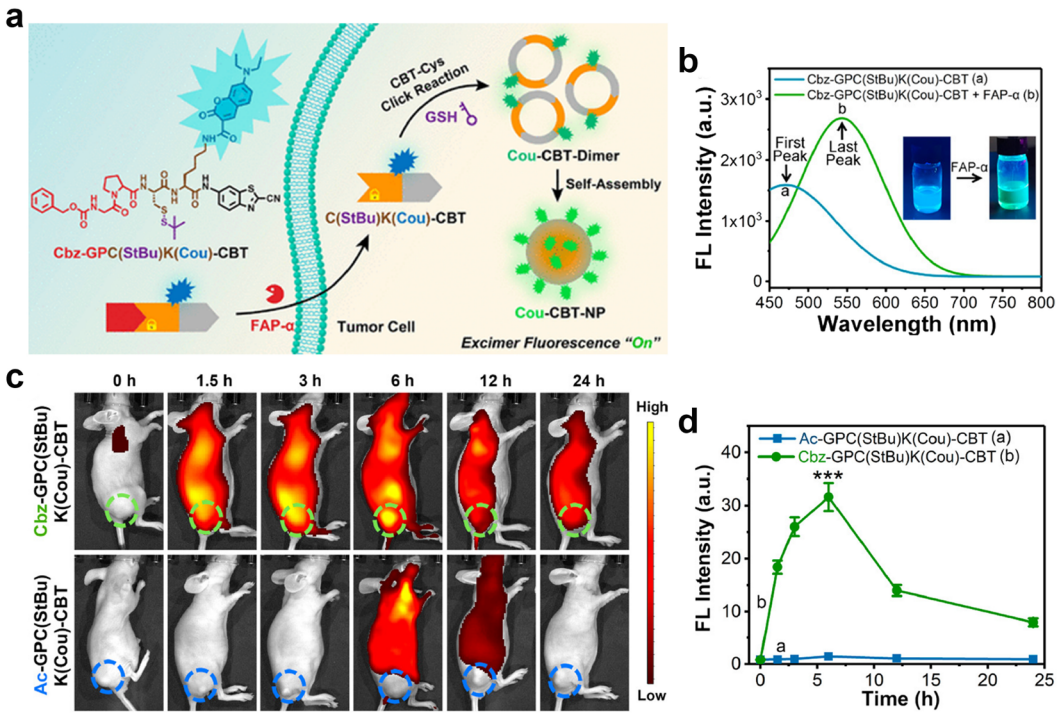

Figure 4. (a) Schematic illustration of the "smart" FAP-α-activatable FL probe **Cbz-GPC(StBu)K(Cou)-CBT** to turn the coumarin excimer fluorescence "on" for high-contrast tumor imaging. (b) FL spectra of **Cbz-GPC(StBu)K(Cou)-CBT** treated with (green) or without (blue) FAP-α and TCEP under the above-mentioned conditions. Inset: corresponding photographs of **Cbz-GPC(StBu)K(Cou)-CBT** solutions with (or w/o) FAP-α and TCEP [tris(2-carboxyethyl)phosphine] under 365 nm UV irradiation by a handheld UV lamp. (c) *In vivo* FLI in MIA PaCa-2 tumor-bearing mice after intravenous injection of 5 μmol kg^{-1} of **Cbz-GPC(StBu)K(Cou)-CBT** or **Ac-GPC(StBu)K(Cou)-CBT**. (d) Time course average fluorescence intensities of tumors (dotted circles) of the mice in (c) (mean ± SD, $n = 5$, ***$P < 0.001$). Reproduced with permission from ref 55. Copyright 2022 American Chemical Society.

in aggregates of AIE molecules, neighboring molecules impede their intramolecular rotation, whose restriction of intramolecular rotations can block the nonradiative pathway and thus open up the radiative channel.[44,45] Consequently, the designed AIE fluorescent molecules own feeble or negligible FL emission in diluted solutions while exhibiting robust FL emission when presenting at high concentrations or in aggregated states.[46] The CBT-Cys-like click reactions offer a versatile approach to cross-link molecules within the probe precursor, which leads to the formation of diverse nanostructures. Therefore, this renders CBT-Cys-like click reactions an ideal strategy for the design of AIE probes.[47] In 2017, Liu et al. utilized a classical AIE molecule tetraphenylethene (TPE) to develop an intelligent FLI probe Ac-Arg-Val-Arg-Arg-Cys-(StBu)-Lys(TPE)-CBT [Ac-RVRR-C(StBu)-K(TPE)-CBT, named as compound **1**] (Figure 3a).[48] The constituents of this probe include an Ac-Arg-Val-Arg-Arg peptide sequence that enhances cellular uptake and acts as a substrate recognized by furin, a CBT group used for CBT-Cys click reaction with disulfide Cys groups, and TPE covalently linked to a Lys side chain amino acid exhibiting AIE property. After being cleaved by furin and reduced by endogenous glutathione (GSH), compound **1** transformed into a **1-Cleaved** molecule with the single AIE effect. Then, **1-Cleaved** molecules could condensate into **1-dimers** and further self-assemble into **1-NPs**, both of which own dual AIE effect. The author proposed an Ac-Arg-Val-Arg-Arg-Lys(TPE)-OH, termed **1-ctrl** molecule, to contrast the FL enhancement of single AIE and dual AIE. The results shown in Figure 3b demonstrated that the FL intensity of the dual AIE effect achieved 109-fold enhancement, which was much higher than that of the single AIE effect (63-fold). These results confirm the importance of using CBT-Cys to construct dual AIE-based FL probes for enhancing FL emission. Similarly, this innovative approach leads to an impressive 3.4-fold FL increase in living cells compared with the single AIE control probe **1-ctrl** (Figure 3c). Overall, this study presents the design of an intelligent dual AIE probe that effectively harnesses the AIE characteristics of TPE for controlled activation by furin and GSH. The utilization of this dual AIE "intelligent" strategy holds immense potential in the precise imaging of enzyme activity *in vitro* and *in vivo*.

In addition to utilizing the characteristics of AIE probe, CBT-Cys-like reactions can also be used to combine with the monomer−excimer principle to design FL probes. An excimer is an excited-state dimer formed by the proximity of a single excited-state monomer to the same monomer.[49] Excimer activation produces a specific FL emission that is much longer than the emission wavelength of the corresponding monomer. This large Stokes red shift can also avoid interference from biological background signals.[50] Meanwhile, because of various wavelength emissions of excimer and monomer, this strategy can significantly improve contrast after activation.[51] Kim and co-workers used cysteinyl aspartate-specific proteinase-3 (caspase-3, a reliable biomarker for assessing cell apoptosis[52,53]), recognition peptide sequence (DEVD), and a benzothiazole-based reference molecule (**CV-NH$_2$**) to construct an excimer-based molecular fluorescent probe Ac-DEVD-**NH−CV** for the detection of caspase-3.[54] Upon enzymatic cleavage of the DEVD peptide by caspase-3, the solubility of the obtained probe significantly decreased, which

https://doi.org/10.1021/cbmi.3c00117
Chem. Biomed. Imaging 2024, 2, 98−116

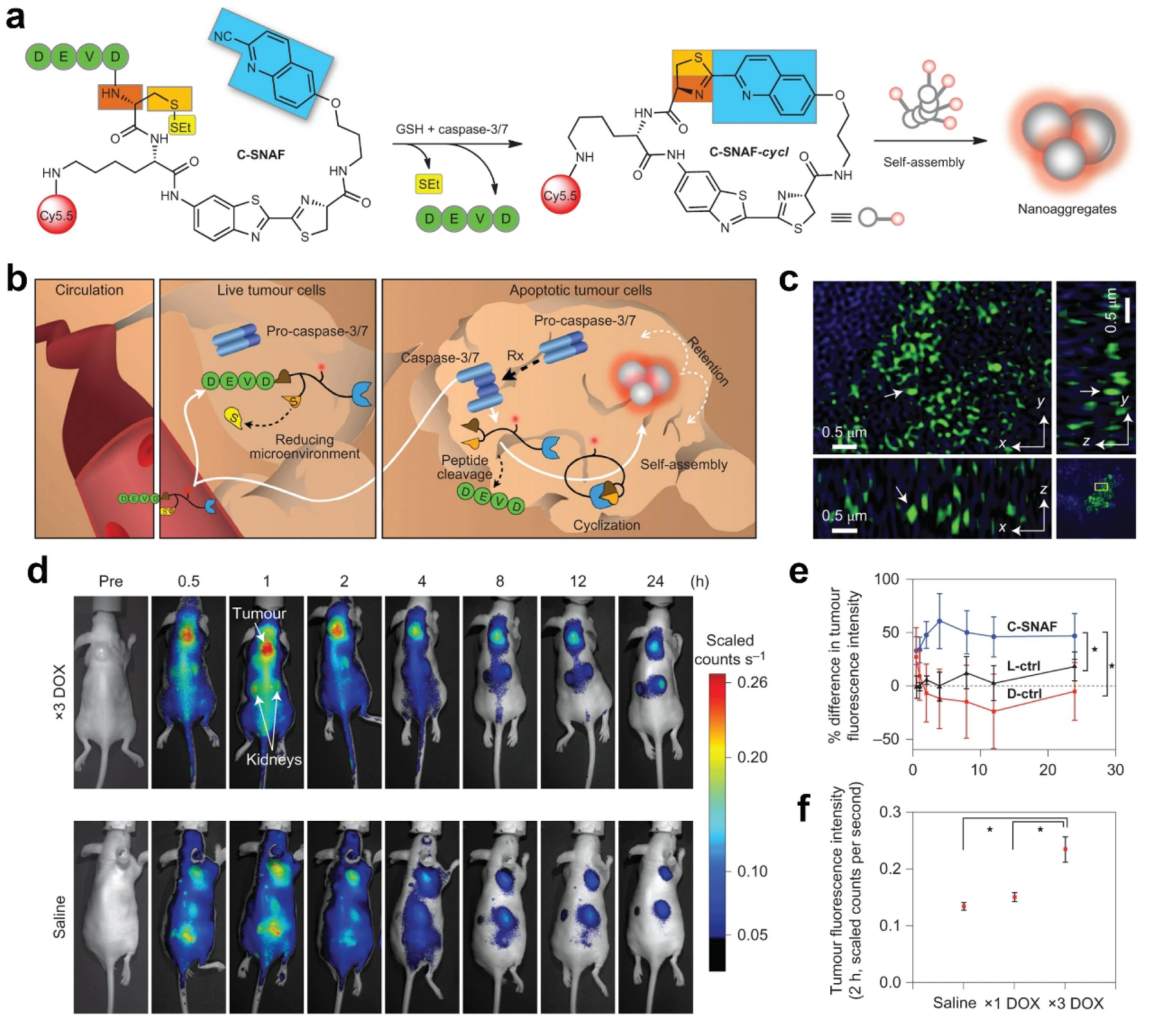

Figure 5. (a) Proposed caspase-3/7 and reduction-controlled conversion of **C-SNAF** into **C-SNAF-*cycl*** through the bioorthogonal intramolecular cyclization reaction followed by self-assembly into nanoaggregates *in situ*. Blue, the CHQ group; dark and light orange, amino and thiol groups of D-cysteine, respectively; yellow, thioethyl masking group; green, the capping peptide residues; red, NIR fluorophore Cy5.5. (b) The fate of **C-SNAF** *in vivo* is dependent on the tumor response to chemotherapy (Rx). After intravenous administration, **C-SNAF** extravasates into tumor tissue because of its small size. In live tumor tissue that does not respond to applied chemotherapy, the pro-caspase-3 is inactive, and the DEVD capping peptide remains intact. **C-SNAF** can diffuse away freely from live tumor tissue, which leads to low fluorescence. In apoptotic tumor tissue, pro-caspase-3 is converted into active caspase-3, and **C-SNAF** can enter cells readily because of the compromised membrane integrity associated with apoptosis. After DEVD cleavage by active caspase-3 and disulfide reduction, **C-SNAF** undergoes macrocyclization and *in situ* nanoaggregation, which leads to enhanced probe retention and high fluorescence. (c) Enlarged 3D-SIM images in a 3D slice of tumor tissues. Arrows show the same fluorescent dots observed in *xy*, *yz*, and *xz* panels. (d) Longitudinal fluorescence imaging with **C-SNAF** (5 nmol) of ×3 DOX-treated (top) and saline-treated (bottom) tumor-bearing mice. Anatomical locations of the tumor and kidneys are indicated by white arrows. Mice that carry subcutaneous HeLa tumors received either iv chemotherapy of 8 mg kg^{-1} of DOX or saline once every 4 days for a total of three times. Two days after the final treatment, **C-SNAF** (5 nmol) in saline was administered iv, and whole-body fluorescence was monitored longitudinally using a Maestro fluorescence imager. (e) The percent difference in tumor fluorescence intensity between ×3 DOX and saline treatment groups over the course of imaging for **C-SNAF** (blue, $n = 5$), **L-ctrl** (black, $n = 5$), and **D-ctrl** (red, $n = 5$). *$P < 0.05$ between groups indicated by brackets. (f) A comparison of the average tumor fluorescence intensity at 2 h after **C-SNAF** administration in saline-treated mice ($n = 4$) or after a ×1 DOX or ×3 DOX treatments in the same animals ($n = 4$). *$P < 0.05$ between groups indicated by brackets. All the error bars indicate standard deviation. Reproduced with permission from ref 57. Copyright 2014 Springer Nature.

resulted in aggregation of **CV-NH$_2$** residues in aqueous solution and subsequent generation of distinctive excimer-based molecular FL. This strategy successfully achieved high-efficiency excimer FLI by inducing hydrophobic aggregation of the probe. In order to further enhance the aggregation effect and, thus, realize better FLI, CBT-Cys-like click reactions have been considered. As it facilitates the formation of cyclic dimers within the probe molecules, the CBT-Cys click cyclization reaction may be an optimal strategy for generating fluorescent chromophores in excimer FL probes. Taking advantage of this characteristic, Gao et al. developed a "smart" fluorescent probe Cbz-Gly-Pro-Cys(StBu)-Lys(coumarin)-CBT [**Cbz-GPC-(StBu)K(Cou)-CBT**] for tumor imaging (Figure 4a).[55] The Cbz-GP peptide sequence within the probe can be enzymatically cleaved by fibroblast activation protein α (FAP-α),[56] which results in the generation of **C(StBu)K(Cou)-CBT**. Subsequently, the reduction of disulfide bonds facilitated by GSH triggers a CBT-Cys click reaction, thereby leading to the

https://doi.org/10.1021/cbmi.3c00117
Chem. Biomed. Imaging 2024, 2, 98−116

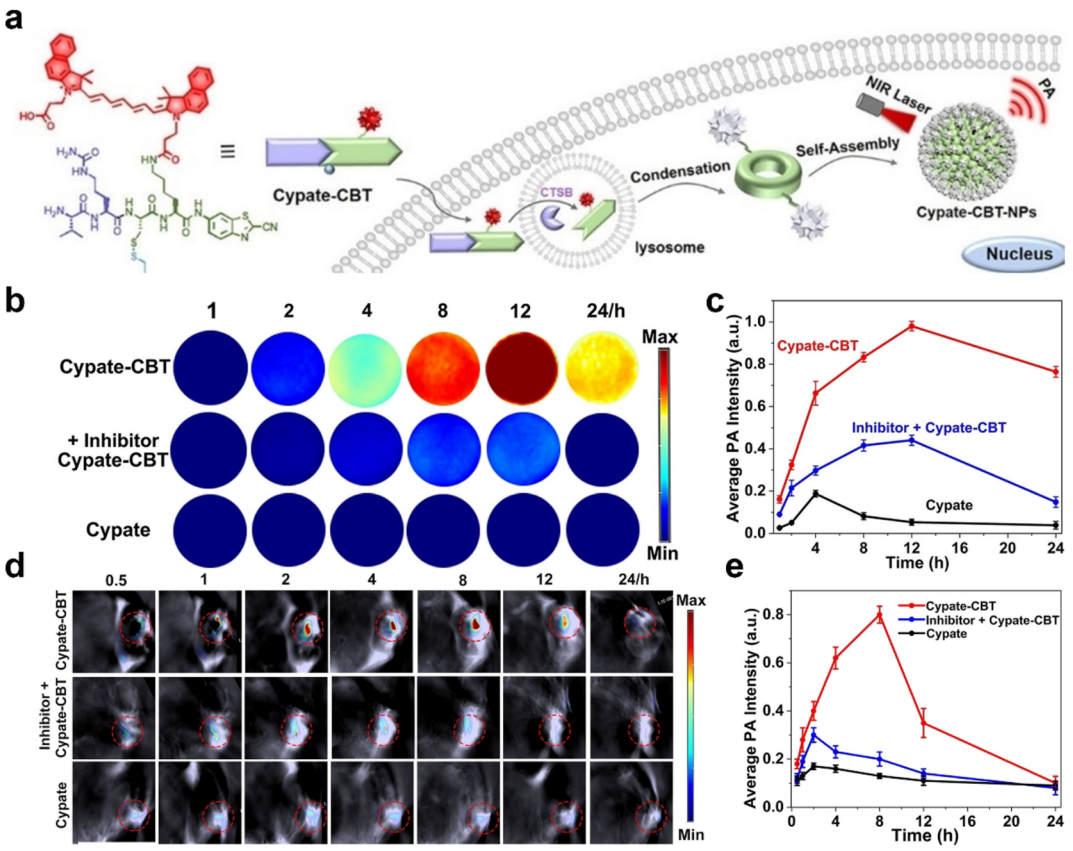

Figure 6. (a) CTSB-triggered self-assembly of **Cypate-CBT-NPs** for PA imaging of CTSB activity *in vitro* and *in vivo*. (b) First row: PA images of MDA-MB-231 cells incubated with 20 μM **Cypate-CBT** for 1, 2, 4, 8, 12, or 24 h, respectively. Middle row: preincubated with 150 μM CA-074-Me for 2 h, then followed by 20 μM **Cypate-CBT** for 1, 2, 4, 8, 12, or 24 h, respectively. Bottom row: incubated with **Cypate** for 1, 2, 4, 8, 12, or 24 h, respectively. MDA-MB-231 cells were detached from culture dishes with trypsin digestion solution after respective incubation and suspended in a serum-free medium with 0.5 wt % agarose gel for detection. (c) Quantified PA intensity of (b). The error bars represent the standard deviation from three separate measurements. Wavelength: 800 nm. (d) Time course PA images of nude mice bearing a MDA-MB-231 tumor after the intratumoral injection of 40 μL of 200 μM **Cypate-CBT** (the first row); intratumoral injection of 20 μL of 40 mM CA-074-Me, followed by 40 μL of 200 μM **Cypate-CBT** 0.5 h later (the middle row); intratumoral injection of 40 μL of 200 μM **Cypate** (the bottom row). The images were acquired at 0.5, 1, 2, 4, 8, 12, or 24 h. (e) Average PA intensity in (d). The error bars represent the standard deviation from three separate measurements. Wavelength: 800 nm. Reproduced with permission from ref 70. Copyright 2021 Wiley-VCH GmbH.

formation of cyclic **Cou-CBT-dimers**. Then, these dimers self-assemble into **Cou-CBT-NPs** through $\pi-\pi$ stacking interactions. As shown in Figure 4b, the unactivated probe displayed a standard Cou monomer FL emission peak at 475 nm. Then, upon FAP-α and reduced substance addition, **Cbz-GPC(StBu)K(Cou)-CBT** molecules were cleaved and further assembled into **Cou-CBT-NPs**, which showed a notable red shift toward a maximum emission wavelength of 550 nm *in vitro*. Remarkable specificity and minimal cytotoxic effects were observed during *in vitro* experiments conducted using this probe. Moreover, *in vivo* imaging studies revealed significantly elevated levels (22-fold increase) of FL intensity at tumor sites compared with control groups (Figure 4c,d). To summarize, the investigation successfully used CBT-Cys reaction to devise an enzyme-activated excimer-based fluorescent probe capable of achieving highly contrasting tumor imaging and exhibited exceptional biocompatibility and potential for effective tumor accumulation, which may offer invaluable insights for clinical diagnosis of FAP-α-associated disorders.

Similarly, CHQ-Cys-based macrocyclic structures are widely applied to FLI. Ye and co-workers synthesized a caspase-3/7-activatable CHQ-Cys-based near-infrared fluorescent probe (**C-SNAF**) to monitor tumor treatment *in vivo* (Figure 5a).[57] **C-SNAF** comprises multiple components: (1) a CHQ and D-Cys moiety for click reaction, along with an amino-fluorescein scaffold for linkage; (2) a DEVD sequence recognized and cleaved by caspase-3/7; and (3) a Cy5.5 fluorophore that emits near-infrared (NIR) fluorescence. Figure 5b illustrates the fate of **C-SNAF** in the body. After intravenous injection, the probe efficiently can penetrate tumor tissue. Through the combined action of GSH and caspase-3/7, the amino group of N-terminal D-Cys becomes exposed to the thiol groups, thereby leading to its reaction with CHQ and subsequent intramolecular cyclization. This process results in the formation of a hydrophobic and rigid macrocyclic compound known as **C-SNAF-*cycl***. The inherent properties of this compound promote molecular aggregation, which facilitates self-assembly into nanoparticles that significantly enhance the retention time of probes within apoptotic cells. The nanoaggregates with ~141 nm diameter could be clearly observed in *ex vivo* tumor tissue (Figure 5c). As shown in Figure 5d, **C-SNAF** showed an excellent tumor retention effect and could reflect the tumor treatment stage in the doxorubicin (DOX, a classical chemotherapeutic drug[58])-treated human cervical carcinoma cell (HeLa) tumor-bearing mice. In comparison with **C-SNAF**, its unassemblable control (**L-ctrl** and **D-ctrl**) exhibited a lower

https://doi.org/10.1021/cbmi.3c00117
Chem. Biomed. Imaging 2024, 2, 98−116

FL intensity *in vivo* (Figure 5e). Finally, animal experiments unequivocally demonstrated that this responsive probe exhibited an augmented DOX-dosage-proportional FL intensity (Figure 5f). Notably, the maximum FL signal closely correlates with changes in tumor size. Consequently, this probe can effectively monitor the response of tumor treatment *in vivo* and facilitate high-contrast imaging to detect changes in tumor treatment response.

Otherwise, to further develop the specificity of CBT-Cys-like click cyclization reaction-based probes, Rao's team devised a proteinase activity pretargeted imaging strategy by integrating two distinct bioorthogonal click reactions (i.e., PMN-Cys reaction and inverse electron demand Diels−Alder reaction).[59] The precursor probe *trans*-cyclooctene (**TCO**)-**C-SNAT4** is linked at the N-terminus to the DEVD sequence, which can be selectively activated by caspase-3/7. Upon activation, the precursor probe undergoes a CBT-Cys-like click condensation reaction to induce intramolecular cyclization and subsequently self-assemble *in situ* into nanoparticles. Following a 30 min injection of **TCO-C-SNAT4**, Tz-Cy5 with a tetrazine structure was administered, thereby enabling Diels−Alder reaction (Tz-TCO) with the *trans*-cyclooctene on **TCO-C-SNAT4** to accomplish enzyme activity pretargeted CBT-Cys-like click imaging.

3.2. Photoacoustic Imaging (PAI)

PAI represents a promising modality that synergistically integrates the outstanding contrast capabilities of optical imaging with the impressive spatial resolution offered by ultrasound.[60,61] Compared with photons, sound waves demonstrate diminished scattering properties within tissues, thereby facilitating deeper penetration into biological structures beyond what can be achieved through conventional FL techniques.[62] This rapidly evolving approach has experienced notable progress in the development of diverse probes for effective cancer detection and therapeutic monitoring.[63−65]

Previous research has demonstrated that PA signals display aggregation-induced enhancement effects, thereby enabling assembled aggregated PA probes to exhibit enhanced performance in PAI.[21,66,67] Gao's team successfully used gold nanoparticles to confirm this perspective.[68] By engineering a light-cross-linked gold nanoparticle, the obtained aggregation exhibited remarkable potential for advancing the fields of PAI and photothermal therapy. Although gold nanomaterials hold potential advantages, their safety profile within the human body remains uncertain.[69] As a consequence, researchers have shifted their attention toward organic self-assembled PA probes as a more secure alternative to address this concern. Recently, Wang et al. developed a PAI probe Val-Cit-Cys(SEt)-Lys(Cypate)-CBT (**Cypate-CBT**) for specific *in vivo* detection of cathepsin B (CTSB) activity (Figure 6a).[70] Upon activation of cellular CTSB, this probe undergoes intermolecular CBT-Cys click reaction to form cyclic dimers, followed by self-assembly of **Cypate-CBT-dimers** through $\pi-\pi$ stacking to result in the formation of **Cypate-CBT-NPs**. Throughout this process, the FL of the probe can be quenched because of the ACQ effect, while the probe's PA signal intensifies with NIR FL quenching. In cellular (Figure 6b,c) and animal experiments (Figure 6d,e), the PA signal of this probe exhibited a remarkable enhancement by 4.9-fold and 4.7-fold, respectively, along with significantly increased accumulation and retention time at tumor sites. In conclusion, this intelligent probe demonstrates promising prospects for application in PAI of overexpressed CTSB in tumors.

Similarly, to image apoptotic regions of tumors *in vivo* for early tumor efficacy assessment, Ye's group originally designed a CHQ-Cys-based caspase-3-responsive self-assembled PA probe.[71] The probe was named **1-RGD**, which was composed of CHQ and D-Cys residues, the caspase-3 cleaved sequence DEVD, the NIR dye indocyanine green (ICG), and a cyclic peptide that increases the tumor-targeting $\alpha_v\beta_3$ integrin receptor (c-RGD). After the probe was internalized by cells, the amino and sulfhydryl groups of D-Cys were exposed under the action of intracellular GSH and caspase-3 and reacted with the CHQ group, which led to intramolecular cyclization. The cyclization products further self-assembled to form nanoparticles because of hydrophobic interaction and $\pi-\pi$ stacking. Because of the ACQ effect, the FL intensity of ICG was weakened and the PA signal was enhanced. *In vivo* imaging results showed the PA signal value of **1-RGD** in DOX-treated tumors reached its maximum value at 10 h, and it was the highest one compared with other treatments. Finally, the authors proved that the PA intensities of **1-RGD** in tumors were correlated with DOX dose. In short, this smart self-assembling probe can be used to detect the apoptosis of tumor cells to realize the early evaluation of tumor therapeutic efficacy.[67] The CBT-Cys-like click cyclization reactions provide design ideas for other PA probes.

3.3. Magnetic Resonance Imaging (MRI)

MRI is an imaging technique that uses the principle of nuclear magnetic resonance (NMR) to map the internal structure of an object by detecting electromagnetic waves emitted by an external gradient magnetic field.[72] It is a noninvasive imaging modality renowned for its exceptional spatial resolution and penetration, which renders it an optimal choice for clinical diagnosis and monitoring of diverse diseases (e.g., cancer and heart disease).[73−75] However, because of its relatively lower sensitivity, the utilization of contrast agents is often necessary to augment its performance.[76] Commonly employed contrast agents can be categorized into longitudinal (spin−lattice) relaxation agents (T_1 agents) and transverse (spin−spin) relaxation agents (T_2 agents).[77] T_1-type contrast agents (e.g., Mn^{2+} and Gd^{3+}) intensify the magnetic resonance signal, thereby resulting in enhanced brightness within the target area.[78] Conversely, T_2-type contrast agents, like superparamagnetic iron oxide (SPIO) particles, significantly abbreviate the transverse relaxation time, which leads to darker lesion areas.[79] A common approach for enhancing the MRI signal is to control the aggregation state of MRI agents. Hence, researchers have proposed the utilization of self-assembled nanomaterials incorporating MRI agents.[80] For example, Hu and co-workers successfully integrated Gd^{3+} into the self-assembling peptide Nap-GFFYGRGD, thereby inducing the formation of supramolecular hydrogels.[81] This complex comprising Gd^{3+} and peptides significantly enhances T_1-weighted MRI performance. Meanwhile, this self-assembly strategy also addresses the problem of a limited duration of body retention for small molecule probes containing Gd^{3+}. Inspired by this work, enzyme-instructed CBT-Cys-like reaction-constructed MRI nanoparticle probes may show greater potential in MRI depending on their stronger assembly ability.

For T_1-weighted MRI, Xu et al. have successfully developed a T_1-weighted MRI probe, **DEVDC$_S$-Gd-CBT**, which can

https://doi.org/10.1021/cbmi.3c00117
Chem. Biomed. Imaging 2024, 2, 98−116

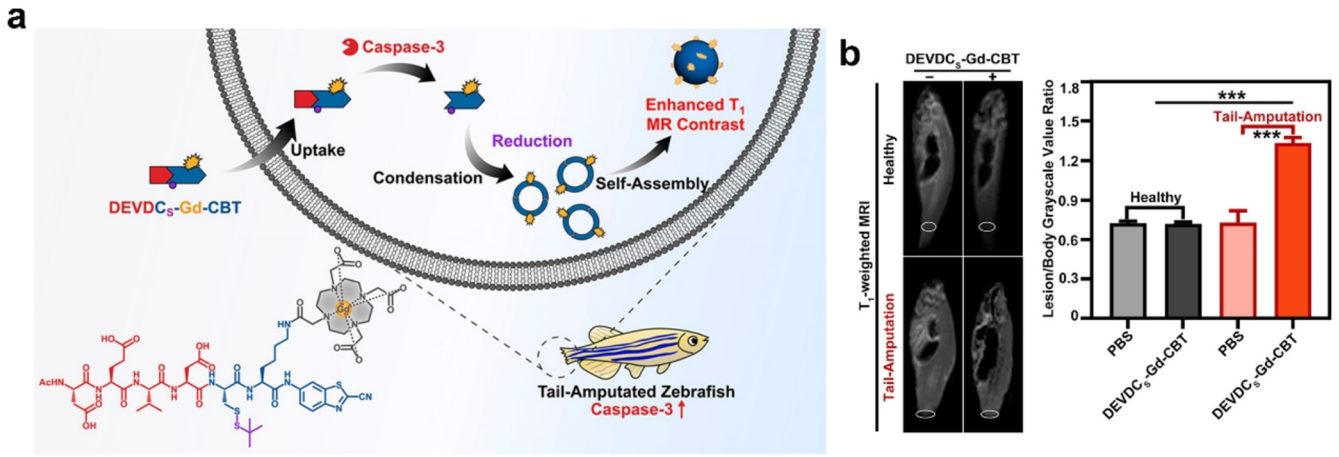

Figure 7. (a) Chemical structures for the probe **DEVDC$_S$-Gd-CBT**, which responds to caspase-3 to form **Gd-NPs** under a reduction condition, and schematic illustration of **DEVDC$_S$-Gd-CBT** for enhanced T_1-weighted MRI of apoptosis in zebrafish. (b) T_1-weighted MR images of zebrafish in the group "Healthy + PBS," group "Tail Amputation + PBS," group "Healthy + **DEVDC$_S$-Gd-CBT**," and group "Tail Amputation + **DEVDC$_S$-Gd-CBT**." Lesion/body grayscale value ratios of MR images (right). Each error bar represents the standard deviation of three independent experiments (mean ± SD, ***P < 0.001). Reproduced with permission from ref 82. Copyright 2023 American Chemical Society.

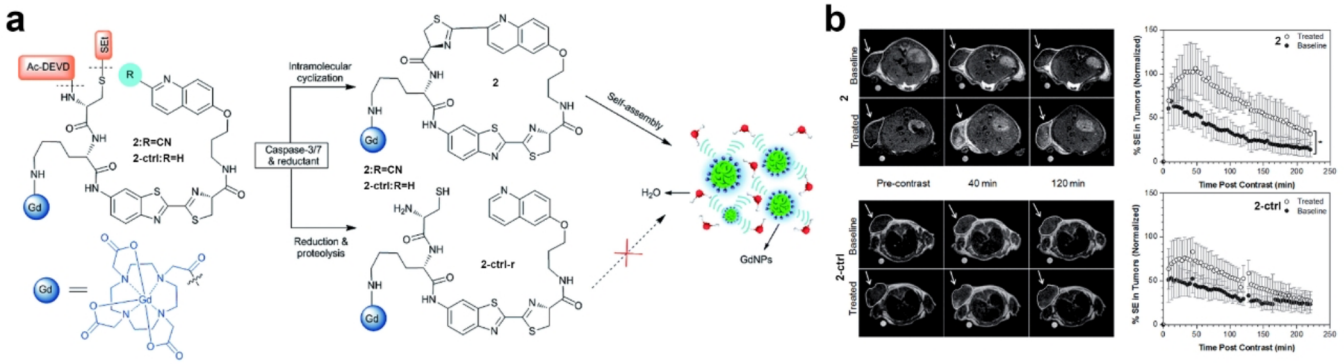

Figure 8. (a) The chemical structures of probe **C-SNAM** (**2**) and its control probe **2-ctrl** and the proposed chemical conversions following disulfide reduction and caspase-3/7-triggered DEVD peptide cleavage. (b) Representative T_1-weighted MR images (1 T) of HeLa tumors prior to (baseline) or following treatment with DOX (treated). Images were obtained before (precontrast) and 40 and 120 min after iv injection of 0.1 mmol kg^{-1} of **2** or **2-ctrl**. The average longitudinal % signal enhancement (% SE) is represented in baseline (●) and treated (○) tumors after iv injection of **2** (n = 8) or **2-ctrl** (n = 4) at 0.1 mmol kg^{-1} dose. The tumor signal intensity (SI) was normalized to the reference standard in a mini-NMR tube (1 mM of Dotarem in PBS), and % SE was calculated at each time point as the % difference between the tumor SI at that time point and the tumor SI in the precontrast (t = 0) data set. *P < 0.05. Error bars are standard deviations. Reproduced with permission from ref 83. Copyright 2014 Royal Society of Chemistry.

utilize the CBT-Cys click reaction to enhance cellular apoptosis imaging and further analyze the tail-amputated zebrafish.[82] As shown in Figure 7a, upon intracellular cleavage by caspase-3 and reduction by GSH, the probe can undergo the CBT-Cys click reaction, thereby leading to the formation of a cyclic dimer and subsequent self-assembly into Gd^{3+} nanoparticles. *In vivo* experiments have convincingly demonstrated significant amplification of T_1-weighted MRI signals of **DEVDC$_S$-Gd-CBT** in apoptosis-activated zebrafish by tail-amputated treatment (Figure 7b). This probe exhibits promising potential for MRI of diseases associated with apoptosis, thereby highlighting its clinical relevance and significance in disease diagnosis and monitoring. Similarly, CHQ-Cys click cyclization reaction can also be applied to enhanced T_1-weighted MRI. Rao's team devised a caspase-3/7-responsive MRI probe (denoted as C-SNAM, **2**) in Figure 8a for effectively monitoring tumor cell apoptosis in mice.[83] Upon intravenous injection of **C-SNAM**, the probe undergoes an intramolecular cyclization reaction triggered by the response of caspase-3/7 and GSH. The cyclized product then self-assembles into **GdNPs**. Notably, the longitudinal relaxivity (r_1) of these Gd^{3+} nanoparticles was approximately 86%, which was higher than that observed with **2** alone. In comparison with control probes, only molecule **2** demonstrates significantly increased longitudinal relaxation enhancement and prolonged retention time specifically within apoptotic tumors (Figure 8b). These findings highlight the potential utility of employing the CBT-Cys-like click reaction-mediated intramolecular cyclization and *in situ* self-assembly as a general design strategy for developing MRI probes capable of assessing enzyme activity *in vivo*.

Compared with T_1 MRI probes based on Gd^{3+}, SPIO-based T_2 MRI probes exhibit superior biocompatibility and safety profiles, thereby rendering them a preferred choice for MRI.[84] Yuan and co-workers developed a CBT-Cys-based aggregable probe for enhanced T_2-weighted MRI.[85] As shown in Figure 9a, they synthesized a small molecule Ac-Asp-Glu-Val-Asp-Cys(StBu)-Lys-CBT (**3**) that could be specifically recognized

https://doi.org/10.1021/cbmi.3c00117
Chem. Biomed. Imaging 2024, 2, 98−116

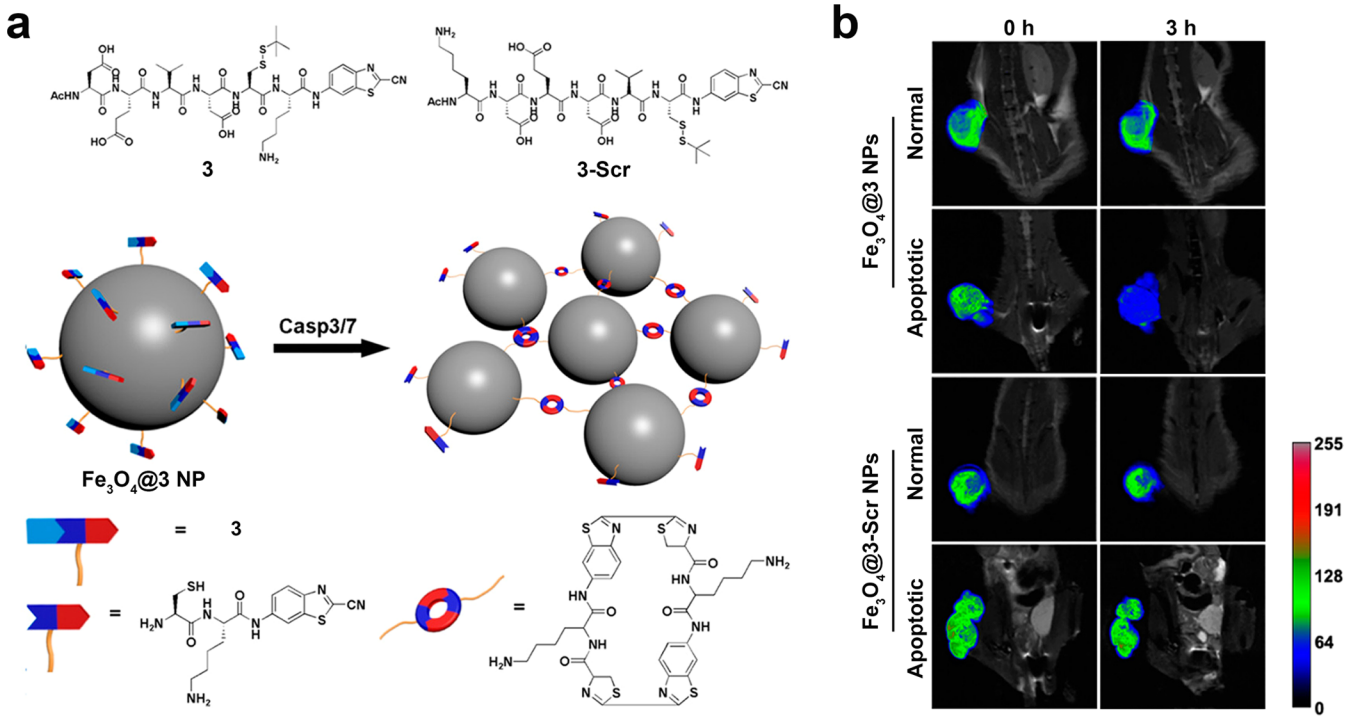

Figure 9. (a) Chemical structures of **3** and **3-Scr** and schematic illustration of intracellular caspase-3/7-instructed aggregation of Fe_3O_4@**3** NPs. (b) *In vivo* T_2-weighted coronal MR images of Fe_3O_4@**3** NPs-injected saline-treated mice, Fe_3O_4@**3** NPs-injected DOX-treated mice, Fe_3O_4@**3-Scr** NPs-injected saline-treated mice, and Fe_3O_4@**3-Scr** NPs-injected DOX-treated mice at 0 h (left) or 3 h postinjection (right). Injection dose: 9.8 mg Fe kg^{-1}. Tumors in the mice were marked with false color to show the significant difference in MR signal intensity. Reproduced with permission from ref 85. Copyright 2016 American Chemical Society.

by caspase-3/7 and covalently modified with ultrasmall SPIO nanoparticles to fabricate monodisperse Fe_3O_4@**3** NPs. Meanwhile, Ac-Lys-Asp-Glu-Asp-Val-Cys(StBu)-CBT (**3-Scr**) was set as a scramble control. Upon interaction with caspase-3/7 and GSH in cells, the CBT-Cys click condensation reaction takes place, which results in the formation of cyclic dimers while cross-linking Fe_3O_4@**3** NPs, thereby transforming them into aggregates with higher transverse relaxivity (r_2) value. Figure 9b shows the T_2 tumor-to-muscle contrast (T/M) ratio with various treatment. The imaging results demonstrate that the change of T/M ratios in apoptotic tumors of human hepatocellular carcinoma (HepG2) cell-bearing mice with Fe_3O_4@**3** NPs injection was much larger than that in normal tumors, while the Fe_3O_4@**3-Scr** NPs could not induce any change between the normal and apoptotic tumor tissues. Thus, this probe showed enhanced T_2 imaging and held great promise for clinical MRI applications aimed at monitoring the efficiency of chemotherapy. Similarly, Wang et al. developed and synthesized Ac-Arg-Val-Arg-Arg-Cys(StBu)-Lys-CBT to conjugate with monodispersed carboxyl-decorated SPIO NPs to form SPIO@1NPs with exceptional r_2 value.[86] Compared with traditional SPIO nanoparticles, their SPIO@1NP could specifically realize enzyme-instructed intracellular CBT-Cys-based aggregation in tumor areas and further facilitate precise MRI T_2-imaging-guided photothermal therapy. On the basis of these MRI progresses, the enzyme-instructed CBT-Cys-like reaction technique is useful for the rational synthesis of MRI probes for use in the fields of tumor diagnosis and treatment.

3.4. Positron Emission Tomography (PET)

PET is a nuclear imaging technique extensively employed in clinical disease detection because of its exceptional sensitivity and tissue penetration capabilities.[87] PET imaging necessitates the utilization of positron-emitting radioactive isotopes for labeling probes with commonly utilized radiotracers encompassing ^{18}F, ^{64}Cu, ^{68}Ga, and ^{89}Zr.[88] Among these options, ^{18}F exhibits superior spatial resolution because of its low positron energy levels. Additionally, the physical half-life of ^{18}F is 110 min, which can prolong *in vivo* monitoring time compared with other PET radiotracers, thereby establishing it as the most widely adopted PET radiotracer within clinical practice.[89,90]

Unlike FLI, radioactive probes cannot be influenced by the ACQ effect. Consequently, *in situ* aggregation can effectively enhance their radioactive signal and facilitate high-contrast PET imaging. On the basis of CBT-Cys click reaction, Lin et al. developed an intelligent tracking probe for precise detection of biotin receptor-positive tumors.[91] This probe can specifically bind to the biotin receptor on the surface of the cell membrane and be internalized through biotin receptor-mediated endocytosis. Upon intracellular reduction by GSH, it initiates the CBT-Cys click reaction, forms hydrophobic cyclized dimers, and further assembles into nanoparticles. MicroPET imaging results exhibited higher tissue uptake, improved imaging contrast, and prolonged tumor retention time of this probe. Further, on the basis of the CBT-Cys click reaction, Lin et al. ingeniously designed a bioorthogonal reaction scaffold (**SF**) through meticulous adjustments in the aromaticity and length of the connecting group between CBT and Cys.[92] This innovative scaffold effectively mitigates the competition posed by free Cys within cells, thereby enabling enhanced efficiency of the probe *in situ* self-assembly and improving imaging performance. On the basis of the scaffold **SF**, the authors synthesized two PET imaging probes, [^{18}**F**]**SF-DEVD** (Figure 10a) and [^{18}**F**]**SF-Glu** (Figure 10e), capable of monitoring

https://doi.org/10.1021/cbmi.3c00117
Chem. Biomed. Imaging 2024, 2, 98−116

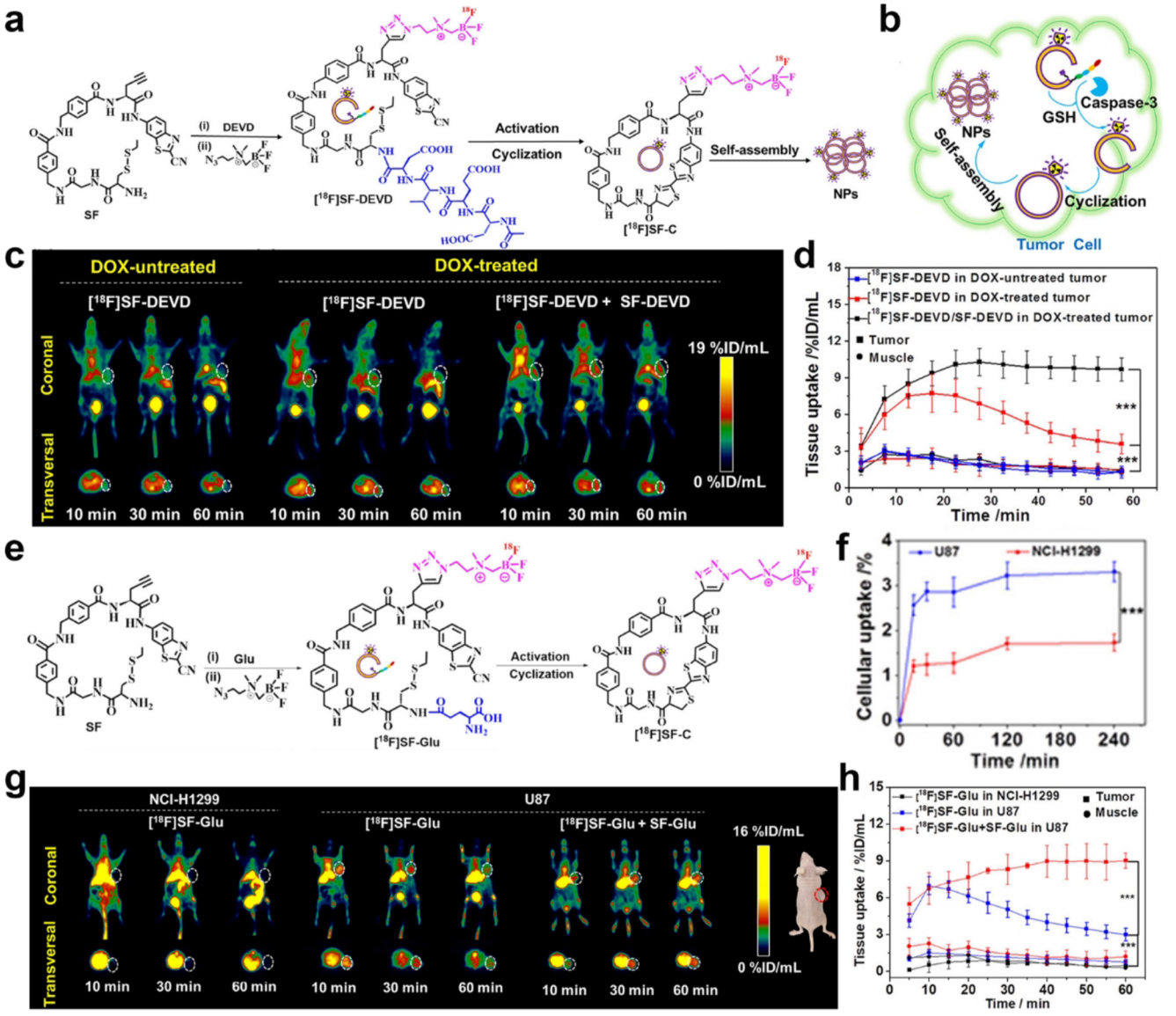

Figure 10. (a) Synthesis and chemical structure of probe [^{18}F]**SF-DEVD** and proposed possible self-assembly mechanism of the probe. (b) Proposed action mechanism of [^{18}F]**SF-DEVD** for detecting caspase-3 activity in tumor cells. (c) Transversal and coronal PET images of HeLa-tumor-bearing mice from 10 to 60 min. (d) Time course of tumor and muscle uptake of [^{18}F]**SF-DEVD** in the mice with or without DOX treatment. (e) Synthesis and chemical structure of tracer [^{18}F]**SF-Glu**. (f) Cellular uptake assay of probe [^{18}F]**SF-Glu** in U87 and NCI-H1299 cells. (g) Transversal and coronal PET images of U87- and NCI-H1299-tumor-bearing mice from 10 to 60 min. (h) Time course of tumor and muscle uptake of [^{18}F]**SF-Glu** in U87- and NCI-H1299-tumor-bearing mice (n = 3). ***P < 0.001. Reproduced with permission from ref 92. Copyright 2022 American Chemical Society.

caspase-3 and γ-glutamyl transpeptidase (GGT) activity, respectively. Figure 10b shows the fate of [^{18}F]**SF-DEVD** in the cells. As shown in Figure 10c, the *in vivo* [^{18}F]**SF-DEVD** radioactive signal intensity of the DOX-treated HeLa tumor-bearing mice was stronger than that of the DOX-untreated one. Further, coinjection with nonradioactive probes (**SF-DEVD**) significantly prolonged the retention of the [^{18}F]**SF-DEVD** probes at the tumor site. In Figure 10d, the tumor drug uptake of DOX-treated tumors in the coinjection group increased 2.85-fold compared with the [^{18}F]**SF-DEVD** injection group at 60 min. However, [^{18}F]**SF-Glu** showed more uptake in human malignant glioblastoma (U87) cells than in human nonsmall-cell lung cancer (NCI-H1299) cells because of the higher GGT expression (Figure 10f), which suggested that [^{18}F]**SF-Glu** can selectively accumulate in tumor cells with high GGT expression. MicroPET scanning results in Figure 10g,h further confirmed that the [^{18}F]**SF-Glu** radioactive signal of U87 tumor-bearing mice reached its maximum signal at 10 min, and this signal strength in the coinjection group could be extended to 60 min, while throughout the process, NCI-H1299 tumor-bearing mice showed little visible radioactive signal. In summary, in comparison with the control group, both of the two probes exhibited enhanced tumor accumulation and contrast, which may contribute to accurately measuring the activity of enzymes in the body. Hence, this smart scaffold **SF** demonstrates its potential as a versatile molecular framework for developing other enzyme-responsive imaging probes. It greatly increases

https://doi.org/10.1021/cbmi.3c00117
Chem. Biomed. Imaging 2024, 2, 98−116

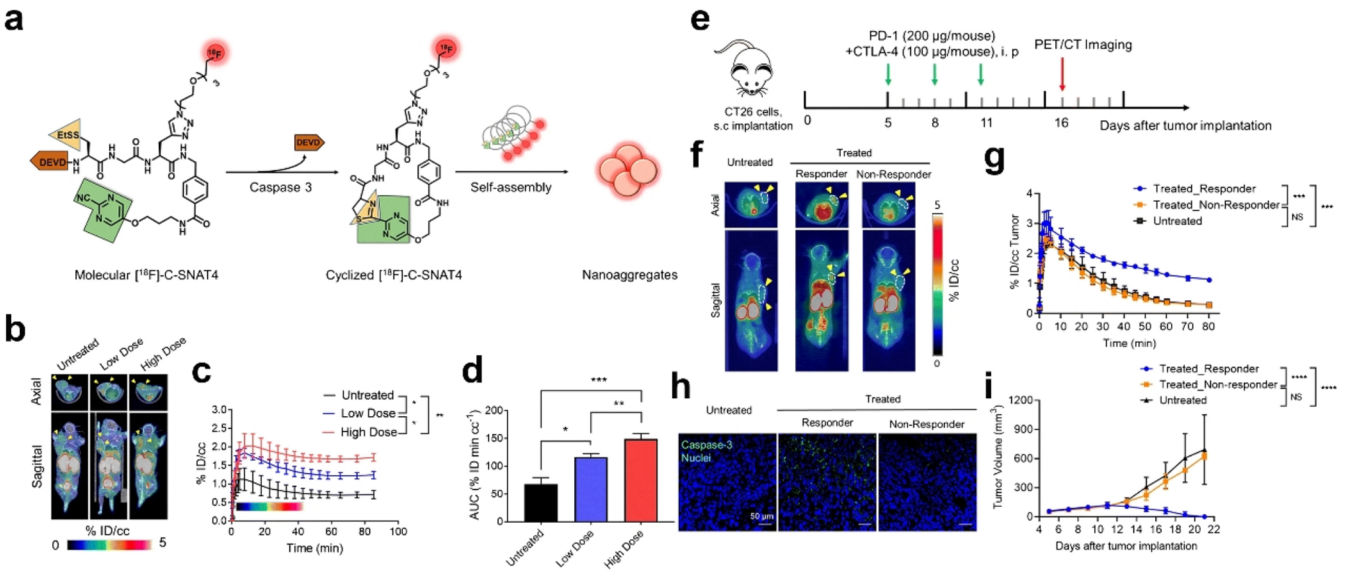

Figure 11. (a) The chemical structure of [^{18}F]-**C-SNAT4** and proposed caspase-3/7 and reduction-controlled conversion of molecular **C-SNAT4** into cyclized [^{18}F]-**C-SNAT4** through the caspase-3-targeted enable *in situ* ligand aggregation, followed by self-assembly into nanoaggregates. Green, the pyrimidine nitrile group; yellow, thiol groups of D-cysteine; brown, the capping peptide residues; red, radiolabel ^{18}F. (b) Representative 55 to 60 min axial and sagittal PET/CT images. Nude mice received 7.4 MBq (200 μCi) of [^{18}F]-**C-SNAT4** via intravenous injections. Yellow arrowheads indicate the tumors identified from the CT images. NCI-H460 tumor-bearing mice were imaged at 24 h following the last dose of cisplatin treatment (low dose, 3 mg kg^{-1}; high dose, 9 mg kg^{-1} every other day for three times). (c) Time−activity curve (TAC) of [^{18}F]-**C-SNAT4** in untreated and drug-treated tumors. Data are mean ± SD, $*P < 0.05$, $**P < 0.01$ (general linear repeated measures), $n = 4$ per group. (d) The area under the curve (AUC) is shown from $t = 0$ to 85 min for TAC in (c). Data are mean ± SD, $*P < 0.05$, $**P < 0.01$, $***P < 0.001$ (ANOVA), $n = 4$ per group. (e) Treatment and imaging timeline in BALB/c mice bearing CT26 tumors. Mice were intraperitoneally injected with 200 μg of PD-1 and 100 μg of CTLA-4 on days 5, 8, and 11 post-CT26 tumor implantation, and PET images were acquired on day 16 post-tumor implantation. (f) Representative axial and sagittal PET images were acquired at 60 min postinjection of [^{18}F]-**C-SNAT4**. Yellow arrowheads indicate the tumors identified from the CT images. (g) Time−activity curve (TAC) for dynamic update of [^{18}F]-**C-SNAT4** in CT26 tumors. Data are mean ± SD, $***P < 0.001$ (general linear model repeated measures), $n = 4$ for each group. (h) *Ex vivo* evaluation of caspase-3 activity by immunofluorescence. Tissue sections are shown at 20× objective. Nuclei = blue, caspase-3 = green; scale bars: 50 μm. (i) Caliper measurements of CT26 tumor volumes in untreated or treated mice. Measurements were recorded over 21 days after tumor implantation. Data are mean ± SD, $****P < 0.0001$ (general linear model repeated measures). NS = not statistically significant. $n = 5$ for each group. Reproduced with permission from ref 94. Copyright 2021 Springer Nature.

the application of CBT-Cys-like click reactions in the field of imaging.

Additionally, Rao's team successfully synthesized a ^{18}F-labeled caspase-3-sensitive PET probe [^{18}F]**C-SNAT** to trace the caspase-3 activity.[93] Following treatment with DOX in HeLa tumor-bearing mice, apoptosis occurred in tumor cells leading to a significant upregulation of caspase-3 expression. Consequently, the probe becomes activated and undergoes a CHQ-Cys click reaction, which results in the formation of a macrocyclic compound. These macrocyclic products subsequently assemble into nanoparticles that not only prolong the retention time of the probe within tumors but also enhance PET signal intensity. Next, Rao's team successfully synthesized another PET probe [^{18}F]**C-SNAT4** that exhibits a response to caspase-3 through the PMN-Cys click cyclization reaction (Figure 11a).[94] This probe undergoes cyclization after intracellular caspase-3 activation and then forms nanoaggregates through hydrophobic interactions. The probe exhibited excellent *in vivo* PET imaging performance for monitoring cisplatin-induced chemotherapy effects, as depicted in Figure 11b,c. It demonstrated rapid accumulation of [^{18}F]**C-SNAT4** in the tumor, thereby achieving maximum signal intensity within a short duration. Furthermore, the radioactive signal of [^{18}F]**C-SNAT4** displayed a positive correlation with cisplatin dose and exhibited prolonged residence time within the tumor (Figure 11d). On the basis of this discovery, the authors further evaluated the potential of [^{18}F]**C-SNAT4** for imaging tumor responses to checkpoint inhibitor immunotherapy. The steps of establishing an immune-checkpoint-inhibited mouse model are shown in Figure 11e. After the intravenous administration of probes, a notable radioactive signal was observed at the tumor site in the treated responder group, whereas little uptake of the probe was detected in both the untreated group and the nonresponder group (Figure 11f,g). In *ex vivo* immunofluorescence analysis, the treated responder had the highest cleaved caspase-3 activity in comparison with the nonresponder and untreated group (Figure 11h). In addition, only in the treated responder group could the tumor size be completely suppressed (Figure 11i). All these results indicate that [^{18}F]**C-SNAT4** can be used to distinguish responders from nonresponders in immunotherapy. This PMN-CBT-based probe shows remarkable potential for clinical applications because of its commendable serum stability, exceptional selectivity toward apoptotic cells, and superior T/M ratio.

In addition to ^{18}F, other metallic radiopharmaceuticals, such as ^{68}Ga, are increasingly utilized in PET imaging because of their ability to be generated via generators, thereby eliminating the necessity for cyclotrons and rendering them easily accessible and more cost-effective.[95] Wang et al. devised a tumor furin-activated PET probe Acetyl-Arg-Val-Arg-Arg-Cys(StBu)-Lys(DOTA-^{68}Ga)-CBT (**CBT-^{68}Ga**).[96] As shown

https://doi.org/10.1021/cbmi.3c00117
Chem. Biomed. Imaging 2024, 2, 98−116

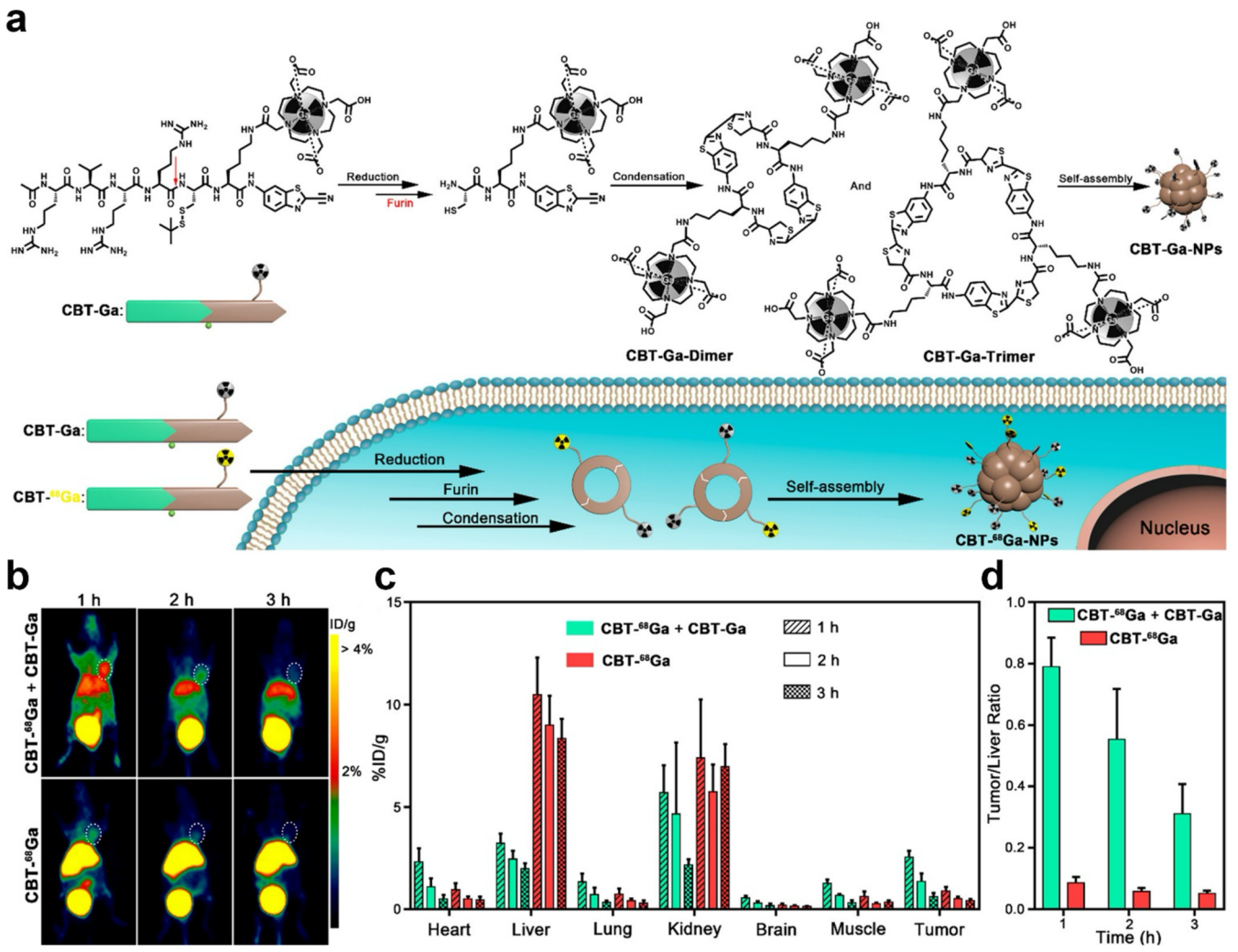

Figure 12. (a) Schematic illustrations of furin-guided Ga nanoparticles formation. After reduction and furin cleavage, **CBT-Ga** is subjected to the CBT-Cys click condensation reaction to yield the cyclized oligomers, which self-assemble into Ga nanoparticles **CBT-Ga-NPs**. Schematic illustrations are also present of furin-controlled condensation of **CBT-^{68}Ga** and **CBT-Ga** to yield hybrid oligomers, which self-assemble into radioactive nanoparticles **CBT-^{68}Ga-NPs** in furin-overexpressing cancer cells. (b) Representative whole body coronal microPET images of MDA-MB-468 tumor-bearing mice at different time points postintravenous injections of 100 μL of 5−12 MBq of **CBT-^{68}Ga** and 20 mg kg^{-1} of **CBT-Ga** (top) or 5−12 MBq of **CBT-^{68}Ga** (bottom) via tail veins. White dashed ellipses indicate the tumors. (c) Time course uptake of **CBT-^{68}Ga** in heart, liver, lung, kidney, brain, muscle, and MDA-MB-468 tumor. The data were derived from PET quantification [% injected dose (ID)/g, n = 4 for each group]. (d) Time course bar graphs of the tumor/liver ratios in part (c). Reproduced with permission from ref 96. Copyright 2019 American Chemical Society.

in Figure 12a, after the cleavage by the furin, the probe undergoes a CBT-Cys click condensation reaction, which results in the formation of cyclic oligomers (dimers or trimers) that subsequently self-assemble into nanoparticles. Non-radiocompound (**CBT-Ga**) can be coinjected with **CBT-^{68}Ga** to ensure that the probe **CBT-^{68}Ga** can better self-assemble in the tumor. Compared with **CBT-^{68}Ga** injection alone, the coinjection group showed higher tumor uptake, which enabled clear tumor imaging, lower liver uptake and retention, and improved imaging contrast (Figure 12b,c). It also showed a higher tumor−liver ratio (Figure 12d). Hence, the CBT-Cys-like reaction can also be used to enhance Ga-based PET bioimaging, and combined with the corresponding nonradiocompound, the CBT-Cys-like-based PET probe may thus provide stronger contrast information in the region of interest. All in all, we wish that more and more other PET radiotracers could be employed to construct CBT-Cys-like probes for enhanced PET imaging.

3.5. Multimodality Imaging

Multimodality imaging combines two or more imaging modalities and produces more imaging details than conventional single-modal imaging,[97] which have received extensive attention and applications.[98] Through integrating various imaging agents, CBT-Cys-like reaction-constructed probes have shown a wonderful bimodal imaging effect in various applications. Ye's team used IR-780 (a NIR FL and PA probe) as a scaffold to conjugate the CHQ, Cys, and DOTA-Gd for the construction of a smart PA/MRI bimodal probe **Gd-IR780** for the apoptosis imaging of tumor cells (Figure 13a).[99] This **Gd-IR780** probe comprises IR780 and DOTA-Gd chelate, which enables the simultaneous acquisition of PA and MRI signals. In apoptotic tumor cells, **Gd-IR780** could be activated

https://doi.org/10.1021/cbmi.3c00117
Chem. Biomed. Imaging 2024, 2, 98−116

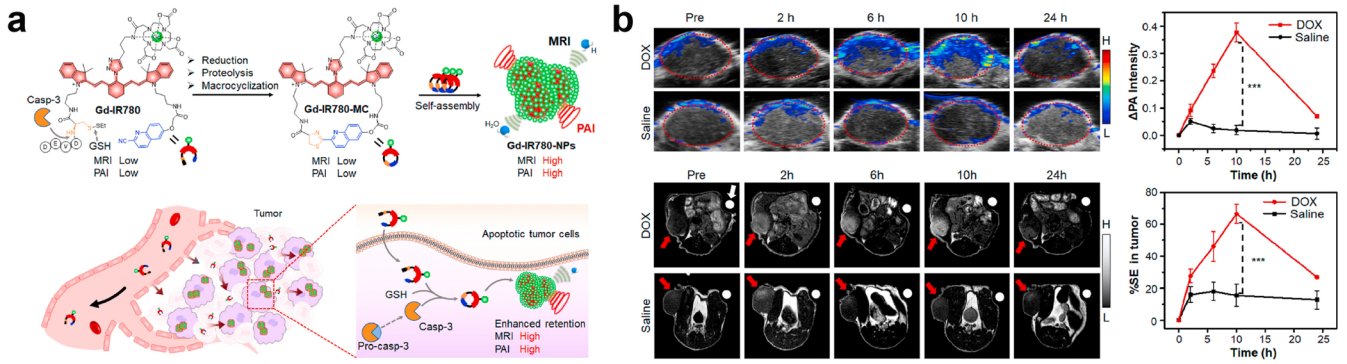

Figure 13. (a) Chemical structure of Gd-IR780 and proposed macrocyclization followed by *in situ* self-assembly into **Gd-IR780-NPs** in response to caspase-3 and GSH and schematic illustration of the mechanism of **Gd-IR780** for bimodal imaging of tumor apoptosis in mice via PAI and MRI. (b) PA images (overlaid with ultrasound images) and PA intensity enhancement (ΔPA) of saline-treated or DOX-treated U87MG tumors in living mice before (Pre) and at 2, 6, 10, and 24 h after iv injection of **Gd-IR780** (0.1 mmol kg^{-1}). PA images were acquired at 855 nm. Values are mean ± SD, ***P < 0.001. Red dashed circles indicate the tumors (top row). Representative T_1-weighted MR images and (g) quantification of % SE in tumors before (Pre) and at 2, 6, 10, and 24 h after iv injection of **Gd-IR780** (0.1 mmol kg^{-1}). Values are mean ± SD (n = 3), ***P < 0.001. Tumors are marked with red arrows. White arrows indicate the Dotarem solution (1 mM) as the internal standard. Reproduced with permission from ref 99. Copyright 2022 Elsevier Ltd.

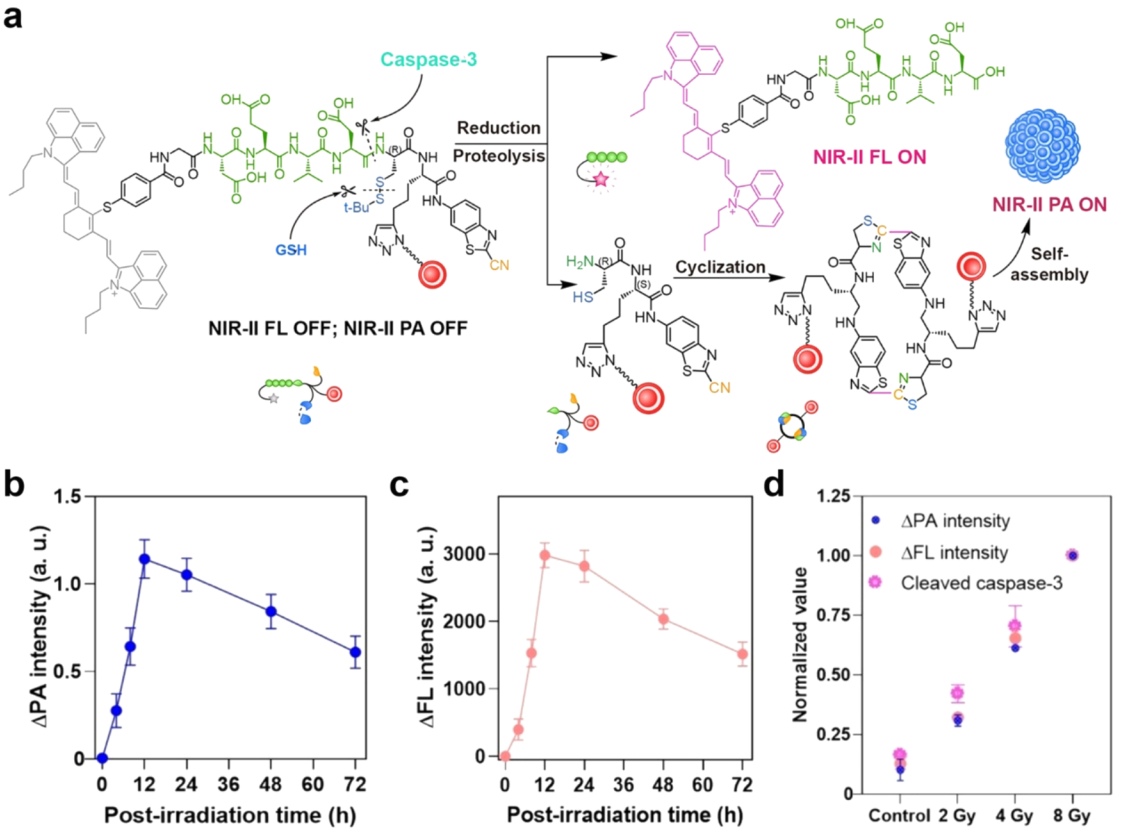

Figure 14. (a) Schematic illustration of caspase-3-mediated release of NIR-II fluorescent (FL) molecule IR-1048 and self-assembly of nanogapped gold nanoparticles (AuNNPs) accompanied by the "turn-on" of FL and photoacoustic (PA) signals. Corresponding imaging ΔPA (b) and ΔFL (c) signals variation curve. (d) Correlation mechanism between the cleaved caspase-3 enzyme expression and the corresponding activated ΔFL (E_x, 808 nm; E_m, 1150 nm) or ΔPA intensity (1250 nm), taken at 12 h after X-ray irradiation with different doses. Reproduced with permission from ref 101. Copyright 2021 Wiley-VCH GmbH.

by caspase-3 and GSH, thereby leading to intramolecular cyclization and the formation of a macrocyclic compound **Gd-IR780-MC**. Subsequently, **Gd-IR780-MC** would self-assemble and further aggregate as **Gd-IR780-NPs**. This aggregation process induces FL quenching and enhances PA signal while restricting molecular rotation for improved r_1 relaxation properties. Meanwhile, nanoparticle formation also extended the retention time of the probe within tumors. *In vivo* experimental results in Figure 13b showed that the apoptosis-activated smart probe **Gd-IR780** could simultaneously amplify PA signals (approximately 4.3-fold) and T_1-weighted MRI signals (around 2.5-fold), thereby enabling high sensitivity and

https://doi.org/10.1021/cbmi.3c00117
Chem. Biomed. Imaging 2024, 2, 98−116

Table 1. Summary of Bioimaging Probes Based on Enzyme-Instructed CBT-Cys-like Click Reactions

probe	enzyme	cyclization type	imaging modalities	reactions type	reference
Cys(StBu)-IEFD-K(Cy5.5)-CBT	granzyme B	intermolecular cyclization	FL	CBT-Cys	41
QMT-CBT	caspase 1	intermolecular cyclization	FL	CBT-Cys	45
Ac-RVRR(StBu)-K(TPE)-CBT	furin	intermolecular cyclization	FL	CBT-Cys	48
Cbz-GPC(StBu)K(Cou)-CBT	FAP-α	intermolecular cyclization	FL	CBT-Cys	55
C-SNAF	caspase-3/7	intramolecular cyclization	FL	CHQ-Cys	57
TCO-C-SNAT4	caspase-3/7	intramolecular cyclization	FL	PMN-Cys	59
NI−C−CBT	nitroreductase	intermolecular cyclization	PA	CBT-Cys	67
Val-Cit-Cys(SEt)-Lys(Cypate)-CBT	cathepsin B	intermolecular cyclization	PA	CBT-Cys	70
1-RGD	caspase-3	intramolecular cyclization	PA	CHQ-Cys	71
$DEVDC_S$-Gd-CBT	caspase-3	intermolecular cyclization	MRI	CBT-Cys	82
C-SNAM	caspase-3/7	intramolecular cyclization	MRI	CHQ-Cys	83
Ac-DEVD-C(StBu)-K-CBT-Fe_3O_4 NPs	caspase-3/7	intermolecular cyclization	MRI	CBT-Cys	85
Ac-RVRR-C(StBu)-K(SPIO)-CBT	furin	intermolecular cyclization	MRI	CBT-Cys	86
[^{18}F]SF-DEVD	caspase-3	intramolecular cyclization	PET	CBT-Cys	92
[^{18}F]SF-Glu	GGT	intramolecular cyclization	PET	CBT-Cys	92
[^{18}F]C-SNAT	caspase-3	intramolecular cyclization	PET	CHQ-Cys	93
[^{18}F]C-SNAT4	caspase-3	intramolecular cyclization	PET	PMN-Cys	94
Ac-RVRR-C(StBu)-K(DOTA-^{68}Ga)-CBT	furin	intermolecular cyclization	PET	CBT-Cys	96
Gd-IR780	caspase-3	intramolecular cyclization	PA/MRI	CHQ-Cys	99
[^{18}F]-IR780−1	caspase-3	intramolecular cyclization	PA/PET	CHQ-Cys	100
AuNNP@DEVD-IR1048	caspase-3	intermolecular cyclization	PA/FL	CBT-Cys	101

spatial resolution imaging of caspase-3 activity *in vivo*. Similarly, the authors used ^{18}F-labeled zwitterionic organotrifluoroborate ([^{18}F]-$AMBF_3$) to replace the DOTA-Gd and conjugated with the same **Cys-IR780-CHQ** scaffold for the construction of a smart PA/PET bimodal probe [^{18}F]**-IR780−1** to monitor tumor cell apoptosis process.[100] Designed [^{18}F]-**IR780−1** can provide an effective tool for the evaluation of the antitumor efficacy at the early stage, which helps provide patients with the optimized therapeutic strategy.

FLI/PAI dual-modal imaging has attracted more and more attention because of its high sensitivity from FLI and high tissue penetration ability from PAI. Song's group developed a caspase-3 activatable NIR-II FL/PA dual-modal probe, IR1048-Asp-Glu-Val-Asp-Cys(StBu)-(nanogapped gold nanoparticles)-CBT (**AuNNP@DEVD-IR1048**) for realizing early evaluation of radiotherapy effect.[101] As shown in Figure 14a, because of the FRET effect, the probe exhibited negligible NIR-II FL and PA signals. Upon the caspase-3 addition, **AuNNP@DEVD-IR1048** could be cleaved into two parts, IR1048-Asp-Glu-Val-Asp and Cys(StBu)-(AuNNP)-CBT. The former could activate NIR-II FL, and the latter underwent CBT-Cys click cyclization reaction under the action of GSH to form dimers and further self-assemble into nanoparticles. Because of the plasma coupling effect between adjacent AuNNPs, NIR-II PA is turned on. The radiotherapeutic evaluation of *in situ* orthotopic liver cancer demonstrated that both signal intensity of NIR-II FL and PA reached the maximum at 12 h after 8 Gy radiotherapeutic treatment (Figure 14b,c). Further, the expressions of caspase-3 were detected under different doses of X-ray irradiation. The results shown in Figure 14d indicated that the irradiation dose, caspase-3 expression, ΔFL intensity, and ΔPA intensity were positively correlated. In conclusion, this caspase-3 activatable NIR-II FL/PA dual-modal probe has high imaging sensitivity and deep tissue penetration, which can be used for early prediction and evaluation of the effect of radiotherapy *in situ*. Overall, the CBT-Cys-like reaction-constructed multimodal probes can realize significant signal enhancement *in situ* with high specificity and sensitivity, which can provide a new idea for the design of efficient bioimaging probes.

4. CONCLUSION AND OUTLOOK

In this review, we introduce in detail the concept and mechanism of CBT-Cys-like click reactions, mainly including CBT-Cys, CHQ-Cys, and PMN-Cys reactions, and present a comprehensive overview of the applications of enzyme-instructed CBT-Cys-like click reactions across diverse imaging modalities. Table 1 classifies and summarizes the important enzyme-instructed CBT-Cys-like click reaction-constructed imaging probes for bioimaging applications. In comparison with alternative imaging strategies, enzyme-instructed CBT-Cys-like click reactions exhibit superior biocompatibility, and their higher second-order reaction rate (i.e., CBT-Cys reaction) or biorthogonality (i.e., CHQ-Cys reaction and PMN-Cys reaction) makes them highly suitable for use in the body. Moreover, the probes can be specifically activated by targeted enzymes in focus, which enables precise imaging of target tissues with enhanced accuracy. Furthermore, *in vivo* cyclization and self-assembly demonstrated by these probes confer dual advantages as both small molecule probes and nanoprobes. In detail, small molecules can easily enter cells and tissues, and then, the larger size of assembled structures formed by *in situ* assembly can effectively reduce probe diffusion, enhance accumulation in target tissues, and significantly prolong retention time in target tissues, thereby improving imaging contrast. In addition, some common distance-dependent nonradiative transfer mechanisms (e.g., ACQ effect, FRET effect, and AIE effect) can be ingeniously utilized by the assembly/disassembly of CBT-Cys-like cyclization for smartly controlling the on−off state of signals. The intelligent design of efficient and multifunctional imaging probes utilizing CBT-Cys-like click reactions has significantly propelled advancements in the field of medical imaging.

Considerable advancements have been made in recent years through the development of imaging probes that utilize enzyme-instructed CBT-Cys-like click reactions. However,

https://doi.org/10.1021/cbmi.3c00117
Chem. Biomed. Imaging 2024, 2, 98−116

there are still significant challenges that require attention. First, the disease microenvironments are often highly complex. It is difficult to achieve precise diagnosis by imaging single enzyme activity. Hence, strategies involving dual or multiple enzyme responses have emerged as current trends in probe design. Second, existing technological limitations impose restrictions on the capabilities of individual imaging modalities. For instance, FLI necessitates addressing concerns regarding tissue penetration depth, while PET imaging requires solutions for low spatial resolution issues. To overcome these limitations and harness the advantages offered by diverse imaging modalities, the design of multimodal imaging probes represents a prudent and effective choice. The third challenge lies in the poor targeting efficiency of small molecules and limitations in real-time monitoring within target areas due to prolonged accumulation time requirements. Therefore, when new probes are developed, more emphasis should be placed on improving targeting ability and real-time monitoring capability. Last but not least, weak targeting can lead to probe accumulation in other healthy tissues and may result in clinical toxicity or side effects. Therefore, further improvements are needed to design new multimodal probes with good targeting efficiency to minimize their impact on healthy tissues. After addressing these concerns, we think that the utilization of enzyme-instructed CBT-Cys-like click reactions to design novel and efficient probes with good targeting ability and multimodal detection functions for precise imaging will greatly advance the field of medical imaging and provide more accurate and comprehensive imaging information support for clinical diagnosis and treatment.

AUTHOR INFORMATION

Corresponding Authors

Xiaofeng Wu − *State Key Laboratory of Digital Medical Engineering, School of Biological Science and Medical Engineering, Southeast University, Nanjing 210096, China*; Email: wuxiaofeng@seu.edu.cn

Gaolin Liang − *State Key Laboratory of Digital Medical Engineering, School of Biological Science and Medical Engineering, Southeast University, Nanjing 210096, China*; orcid.org/0000-0002-6159-9999; Email: gliang@seu.edu.cn

Authors

Yang Yang − *State Key Laboratory of Digital Medical Engineering, School of Biological Science and Medical Engineering, Southeast University, Nanjing 210096, China*

Xiaoyang Liu − *State Key Laboratory of Digital Medical Engineering, School of Biological Science and Medical Engineering, Southeast University, Nanjing 210096, China*; orcid.org/0000-0002-8649-7809

Complete contact information is available at: https://pubs.acs.org/10.1021/cbmi.3c00117

Author Contributions

†Y.Y. and X.L. contributed equally.

Notes

The authors declare no competing financial interest.

ACKNOWLEDGMENTS

This work was supported by the National Natural Science Foundation of China (Grants 22234002 and 22074016) and the Postgraduate Research & Practice Innovation Program of Jiangsu Province (KYCX22_0245).

VOCABULARY

Molecular imaging is a technique based on specific molecular probes and intrinsic tissue features as the sources of images to monitor biological processes at the molecular and cellular levels within living organisms.

Click reaction is a type of reaction with high efficiency, mild conditions, and rapid reaction rate, which was first raised by Sharpless et al. in 2001.

CBT-Cys-like reactions include the CBT-Cys click reaction developed by Liang et al. from the regenerative pathway of D-luciferin in fireflies and its derived reactions (i.e., CHQ-Cys reaction and PMN-Cys reaction).

Fluorescence imaging (FLI) is an optical imaging technique that has gained widespread applications in disease diagnosis because of its exceptional spatiotemporal resolution and noninvasive characteristic.

Photoacoustic imaging (PAI) is an imaging technique that synergistically integrates the outstanding contrast capabilities of optical imaging with the impressive spatial resolution offered by ultrasound imaging.

Magnetic resonance imaging (MRI) is an imaging technique that uses the principle of nuclear magnetic resonance to map the internal structure of an object by detecting electromagnetic waves emitted by an external gradient magnetic field.

Positron emission tomography (PET) is a nuclear imaging technique extensively employed in clinical disease detection because of its exceptional sensitivity and tissue penetration capabilities.

REFERENCES

(1) Willmann, J. K.; van Bruggen, N.; Dinkelborg, L. M.; Gambhir, S. S. Molecular Imaging in Drug Development. *Nat. Rev. Drug Discovery* **2008**, *7*, 591−607.

(2) Wang, W.; Hu, Z. Targeting Peptide-Based Probes for Molecular Imaging and Diagnosis. *Adv. Mater.* **2019**, *31*, No. e1804827.

(3) Razgulin, A.; Ma, N.; Rao, J. Strategies for *In Vivo* Imaging of Enzyme Activity: An Overview and Recent Advances. *Chem. Soc. Rev.* **2011**, *40*, 4186−4216.

(4) Chen, L.; Lyu, Y.; Zhang, X.; Zheng, L.; Li, Q.; Ding, D.; Chen, F.; Liu, Y.; Li, W.; Zhang, Y.; Huang, Q.; Wang, Z.; Xie, T.; Zhang, Q.; Sima, Y.; Li, K.; Xu, S.; Ren, T.; Xiong, M.; Wu, Y.; Song, J.; Yuan, L.; Yang, H.; Zhang, X. B.; Tan, W. Molecular Imaging: Design Mechanism and Bioapplications. *Sci. China Chem.* **2023**, *66*, 1336−1383.

(5) Wu, D.; Yang, K.; Zhang, Z.; Feng, Y.; Rao, L.; Chen, X.; Yu, G. Metal-Free Bioorthogonal Click Chemistry in Cancer Theranostics. *Chem. Soc. Rev.* **2022**, *51*, 1336−1376.

(6) Devaraj, N. K. The Future of Bioorthogonal Chemistry. *ACS Cent. Sci.* **2018**, *4*, 952−959.

(7) Kim, E.; Koo, H. Biomedical Applications of Copper-Free Click Chemistry: *In Vitro*, *In Vivo*, and *Ex Vivo*. *Chem. Sci.* **2019**, *10*, 7835−7851.

(8) Kolb, H. C.; Finn, M. G.; Sharpless, K. B. Click Chemistry: Diverse Chemical Function from a Few Good Reactions. *Angew. Chem., Int. Ed.* **2001**, *40*, 2004−2021.

(9) Hein, J. E.; Fokin, V. V. Copper-Catalyzed Azide-Alkyne Cycloaddition (CuAAC) and Beyond: New Reactivity of Copper(I) Acetylides. *Chem. Soc. Rev.* **2010**, *39*, 1302−1315.

(10) Hou, X.; Ke, C.; Fraser Stoddart, J. Cooperative Capture Synthesis: Yet Another Playground for Copper-Free Click Chemistry. *Chem. Soc. Rev.* **2016**, *45*, 3766−3780.
(11) Jiang, Q.; Zhan, W.; Liu, X.; Bai, L.; Wang, M.; Xu, Y.; Liang, G. Assembly Drives Regioselective Azide-Alkyne Cycloaddition Reaction. *Nat. Commun.* **2023**, *14*, 3935.
(12) Baskin, J. M.; Prescher, J. A.; Laughlin, S. T.; Agard, N. J.; Chang, P. V.; Miller, I. A.; Lo, A.; Codelli, J. A.; Bertozzi, C. R. Copper-Free Click Chemistry for Dynamic *In Vivo* Imaging. *Proc. Nat. Acad. Sci.* **2007**, *104*, 16793−16797.
(13) Liang, G.; Ren, H.; Rao, J. A biocompatible condensation reaction for controlled assembly of nanostructures in living cells. *Nat. Chem.* **2010**, *2*, 54−60.
(14) Wang, Y.; An, R.; Luo, Z.; Ye, D. Firefly Luciferin-Inspired Biocompatible Chemistry for Protein Labeling and *In Vivo* Imaging. *Chemistry* **2018**, *24*, 5707−5722.
(15) Ye, D.; Liang, G.; Ma, M. L.; Rao, J. Controlling Intracellular Macrocyclization for the Imaging of Protease Activity. *Angew. Chem., Int. Ed.* **2011**, *50*, 2275−2279.
(16) Hu, X.; Tang, R.; Bai, L.; Liu, S.; Liang, G.; Sun, X. CBT-Cys Click Reaction for Optical Bioimaging *In Vivo*. *VIEW* **2023**, *4*, No. 20220065.
(17) Liu, H. W.; Chen, L.; Xu, C.; Li, Z.; Zhang, H.; Zhang, X. B.; Tan, W. Recent Progresses in Small-Molecule Enzymatic Fluorescent Probes for Cancer Imaging. *Chem. Soc. Rev.* **2018**, *47*, 7140−7180.
(18) Zhang, J.; Chai, X.; He, X. P.; Kim, H. J.; Yoon, J.; Tian, H. Fluorogenic Probes for Disease-Relevant Enzymes. *Chem. Soc. Rev.* **2019**, *48*, 683−722.
(19) Zeng, Z.; Liew, S. S.; Wei, X.; Pu, K. Hemicyanine-Based Near-Infrared Activatable Probes for Imaging and Diagnosis of Diseases. *Angew. Chem., Int. Ed.* **2021**, *60*, 26454−26475.
(20) Chen, P.; Kuang, W.; Zheng, Z.; Yang, S.; Liu, Y.; Su, L.; Zhao, K.; Liang, G. Carboxylesterase-Cleavable Biotinylated Nanoparticle for Tumor-Dual Targeted Imaging. *Theranostics* **2019**, *9*, 7359−7369.
(21) Dragulescu-Andrasi, A.; Kothapalli, S.-R.; Tikhomirov, G. A.; Rao, J.; Gambhir, S. S. Activatable Oligomerizable Imaging Agents for Photoacoustic Imaging of Furin-Like Activity in Living Subjects. *J. Am. Chem. Soc.* **2013**, *135*, 11015−11022.
(22) Wei, M.; Wang, L.; Wang, Y.; Zhang, T.; Wang, C.; Wu, C.; Tian, C.; Liang, G.; Yuan, Y. Intracellular Construction of Cathepsin B-Guided Gadolinium Nanoparticles for Enhanced T_2-Weighted MR Tumor Imaging. *Small* **2023**, *19*, No. e2300015.
(23) Chen, P.; Wang, H.; Wu, H.; Zou, P.; Wang, C.; Liu, X.; Pan, Y.; Liu, Y.; Liang, G. Intracellular Synthesis of Hybrid Gallium-68 Nanoparticle Enhances MicroPET Tumor Imaging. *Anal. Chem.* **2021**, *93*, 6329−6334.
(24) Wang, Y.; Bai, H.; Miao, Y.; Weng, J.; Huang, Z.; Fu, J.; Zhang, Y.; Lin, J.; Ye, D. Tailoring a Near-Infrared Macrocyclization Scaffold Allows the Control of *In Situ* Self-Assembly for Photoacoustic/PET Bimodal Imaging. *Angew. Chem., Int. Ed.* **2022**, *61*, No. e202200369.
(25) Yuan, Y.; Liang, G. A Biocompatible, Highly Efficient Click Reaction and Its Applications. *Org. Biomol. Chem.* **2014**, *12*, 865−871.
(26) Cui, L.; Vivona, S.; Smith, B. R.; Kothapalli, S. R.; Liu, J.; Ma, X.; Chen, Z.; Taylor, M.; Kierstead, P. H.; Frechet, J. M. J.; Gambhir, S. S.; Rao, J. Reduction Triggered *In Situ* Polymerization in Living Mice. *J. Am. Chem. Soc.* **2020**, *142*, 15575−15584.
(27) Chen, P.; Ma, Y.; Zheng, Z.; Wu, C.; Wang, Y.; Liang, G. Facile Syntheses of Conjugated Polymers for Photothermal Tumour Therapy. *Nat. Commun.* **2019**, *10*, 1192.
(28) Chen, Z.; Chen, M.; Cheng, Y.; Kowada, T.; Xie, J.; Zheng, X.; Rao, J. Exploring the Condensation Reaction between Aromatic Nitriles and Amino Thiols To Optimize *In Situ* Nanoparticle Formation for the Imaging of Proteases and Glycosidases in Cells. *Angew. Chem., Int. Ed.* **2020**, *59*, 3272−3279.
(29) Driggers, E. M.; Hale, S. P.; Lee, J.; Terrett, N. K. The Exploration of Macrocycles for Drug Discovery-An Underexploited Structural Class. *Nat. Rev. Drug Discovery* **2008**, *7*, 608−624.
(30) Li, X.; Gao, X.; Shi, W.; Ma, H. Design Strategies for Water-Soluble Small Molecular Chromogenic and Fluorogenic Probes. *Chem. Rev.* **2014**, *114*, 590−659.
(31) Wang, S.; Ren, W. X.; Hou, J. T.; Won, M.; An, J.; Chen, X.; Shu, J.; Kim, J. S. Fluorescence Imaging of Pathophysiological Microenvironments. *Chem. Soc. Rev.* **2021**, *50*, 8887−8902.
(32) Zhan, W.; Xu, L.; Liu, Z.; Liu, X.; Gao, G.; Xia, T.; Cheng, X.; Sun, X.; Wu, F. G.; Yu, Q.; Liang, G. Tandem Guest-Host-Receptor Recognitions Precisely Guide Ciprofloxacin to Eliminate Intracellular *Staphylococcus Aureus*. *Angew. Chem., Int. Ed.* **2023**, *62*, No. e202306427.
(33) Huang, J.; Pu, K. Activatable Molecular Probes for Second Near-Infrared Fluorescence, Chemiluminescence, and Photoacoustic Imaging. *Angew. Chem., Int. Ed.* **2020**, *59*, 11717−11731.
(34) Charron, D. M.; Zheng, G. Nanomedicine Development Guided by FRET Imaging. *Nano Today* **2018**, *18*, 124−136.
(35) Yang, X.; Wang, Y.; Liu, R.; Zhang, Y.; Tang, J.; Yang, E.-b.; Zhang, D.; Zhao, Y.; Ye, Y. A Novel ICT-Based Two Photon and NIR Fluorescent Probe for Labile Fe^{2+} Detection and Cell Imaging in Living Cells. *Sensor. Actuat. B-Chem.* **2019**, *288*, 217−224.
(36) Zhao, Y.; Hai, Z.; Wang, H.; Su, L.; Liang, G. Legumain-Specific Near-Infrared Fluorescence "Turn On" for Tumor-Targeted Imaging. *Anal. Chem.* **2018**, *90*, 8732−8735.
(37) Du, W.; Chong, Y.; Hu, X.; Wang, Y.; Zhu, Y.; Chen, J.; Li, X.; Zhang, Q.; Wang, G.; Jiang, J.; Liang, G. Increasing Photothermal Efficacy by Simultaneous Intra- and Intermolecular Fluorescence Quenching. *Adv. Funct. Mater.* **2020**, *30*, No. 1908073.
(38) Li, Y.; Liu, S.; Ni, H.; Zhang, H.; Zhang, H.; Chuah, C.; Ma, C.; Wong, K. S.; Lam, J. W. Y.; Kwok, R. T. K.; Qian, J.; Lu, X.; Tang, B. Z. ACQ-to-AIE Transformation: Tuning Molecular Packing by Regioisomerization for Two-Photon NIR Bioimaging. *Angew. Chem., Int. Ed.* **2020**, *132*, 12922−12926.
(39) Huang, M.; Yu, R.; Xu, K.; Ye, S.; Kuang, S.; Zhu, X.; Wan, Y. An Arch-Bridge-Type Fluorophore for Bridging the Gap Between Aggregation-Caused Quenching (ACQ) and Aggregation-Induced Emission (AIE). *Chem. Sci.* **2016**, *7*, 4485−4491.
(40) Xu, L.; Zhan, W.; Deng, Y.; Liu, X.; Gao, G.; Sun, X.; Liang, G. ROS Turn Nanoparticle Fluorescence on for Imaging *Staphylococcus Aureus* Infection *In Vivo*. *Adv. Healthcare Mater.* **2022**, *11*, No. e2200453.
(41) Xu, L.; Liu, N.; Zhan, W.; Deng, Y.; Chen, Z.; Liu, X.; Gao, G.; Chen, Q.; Liu, Z.; Liang, G. Granzyme B Turns Nanoparticle Fluorescence "On" for Imaging Cytotoxic T Lymphocyte Activity in Vivo. *ACS Nano* **2022**, *16*, 19328−19334.
(42) Luo, J.; Xie, Z.; Lam, J. W. Y.; Cheng, L.; Chen, H.; Qiu, C.; Kwok, H. S.; Zhan, X.; Liu, Y.; Zhu, D.; Tang, B. Z. Aggregation-Induced Emission of 1-methyl-1,2,3,4,5-pentaphenylsilole. *Chem. Commun.* **2001**, 1740−1741.
(43) Chen, Y.; Lam, J. W. Y.; Kwok, R. T. K.; Liu, B.; Tang, B. Z. Aggregation-Induced Emission: Fundamental Understanding and Future Developments. *Mater. Horiz.* **2019**, *6*, 428−433.
(44) Hong, Y.; Lam, J. W. Y.; Tang, B. Z. Aggregation-Induced Emission: Phenomenon, Mechanism and Applications. *Chem. Commun.* **2009**, 4332−4353.
(45) Xu, L.; Gao, H.; Zhan, W.; Deng, Y.; Liu, X.; Jiang, Q.; Sun, X.; Xu, J.-J.; Liang, G. Dual Aggregations of a Near-Infrared Aggregation-Induced Emission Luminogen for Enhanced Imaging of Alzheimer's Disease. *J. Am. Chem. Soc.* **2023**, *145*, 27748−27756.
(46) Hong, Y.; Lam, J. W. Y.; Tang, B. Z. Aggregation-Induced Emission. *Chem. Soc. Rev.* **2011**, *40*, 5361−5388.
(47) Zhang, M.; Liang, G. Applications of CBT-Cys Click Reaction: Past, Present, and Future. *Sci. China Chem.* **2018**, *61*, 1088−1098.
(48) Liu, X.; Liang, G. Dual Aggregation-Induced Emission for Enhanced Fluorescence Sensing of Furin Activity *In Vitro* and in Living Cells. *Chem. Commun.* **2017**, *53*, 1037−1040.
(49) Valeur, B.; Leray, I. Design Principles of Fluorescent Molecular Sensors for Cation Recognition. *Coordin. Chem. Rev.* **2000**, *205*, 3−40.
(50) Zhong, Y.; Zhan, J.; Xu, G.; Chen, Y.; Qin, Q.; Liao, X.; Ma, S.; Yang, Z.; Cai, Y. Enzyme-Instructed Self-Assembly Enabled

Monomer-Excimer Transition to Construct Higher Ordered Luminescent Supramolecular Assembly for Activity-Based Bioimaging. *Angew. Chem., Int. Ed.* **2021**, *60*, 8121−8129.
(51) Chen, Y. Recent Advances in Excimer-Based Fluorescence Probes for Biological Applications. *Molecules* **2022**, *27*, 8628.
(52) Liu, X.; Zhan, W.; Gao, G.; Jiang, Q.; Zhang, X.; Zhang, H.; Sun, X.; Han, W.; Wu, F. G.; Liang, G. Apoptosis-Amplified Assembly of Porphyrin Nanofiber Enhances Photodynamic Therapy of Oral Tumor. *J. Am. Chem. Soc.* **2023**, *145*, 7918−7930.
(53) Wang, P.; Yang, H.; Liu, C.; Qiu, M.; Ma, X.; Mao, Z.; Sun, Y.; Liu, Z. Recent Advances in the Development of Activatable Multifunctional Probes for *In Vivo* Imaging of Caspase-3. *Chin. Chem. Lett.* **2021**, *32*, 168−178.
(54) Kim, T. I.; Jin, H.; Bae, J.; Kim, Y. Excimer Emission-Based Fluorescent Probe Targeting Caspase-3. *Anal. Chem.* **2017**, *89*, 10565−10569.
(55) Gao, G.; Sun, X.; Liu, X.; Tang, R.; Wang, M.; Zhan, W.; Zheng, J.; Liang, G. FAP-α-Instructed Coumarin Excimer Formation for High Contrast Fluorescence Imaging of Tumor. *Nano Lett.* **2022**, *22*, 6782−6786.
(56) Song, P.; Pan, Q.; Sun, Z.; Zou, L.; Yang, L. Fibroblast Activation Protein Alpha: Comprehensive Detection Methods for Drug Target and Tumor Marker. *Chem. Biol. Interact.* **2022**, *354*, No. 109830.
(57) Ye, D.; Shuhendler, A. J.; Cui, L.; Tong, L.; Tee, S. S.; Tikhomirov, G.; Felsher, D. W.; Rao, J. Bioorthogonal Cyclization-Mediated *In Situ* Self-Assembly of Small-Molecule Probes for Imaging Caspase Activity *In Vivo*. *Nat. Chem.* **2014**, *6*, 519−526.
(58) Chen, X.; Zhang, X.; Guo, Y.; Zhu, Y. X.; Liu, X.; Chen, Z.; Wu, F. G. Smart Supramolecular "Trojan Horse"-Inspired Nanogels for Realizing Light-Triggered Nuclear Drug Influx in Drug-Resistant Cancer Cells. *Adv. Funct. Mater.* **2019**, *29*, No. 1807772.
(59) Chen, Z.; Chen, M.; Zhou, K.; Rao, J. Pre-Targeted Imaging of Protease Activity through *In Situ* Assembly of Nanoparticles. *Angew. Chem., Int. Ed.* **2020**, *59*, 7864−7870.
(60) Wang, L. V.; Yao, J. A Practical Guide to Photoacoustic Tomography in the Life Sciences. *Nat. Methods* **2016**, *13*, 627−638.
(61) Wang, L. V.; Hu, S. Photoacoustic Tomography: *In Vivo* Imaging from Organelles to Organs. *Science* **2012**, *335*, 1458−1462.
(62) Beard, P. Biomedical Photoacoustic Imaging. *Interface Focus* **2011**, *1*, 602−631.
(63) Weber, J.; Beard, P. C.; Bohndiek, S. E. Contrast Agents for Molecular Photoacoustic Imaging. *Nat. Methods* **2016**, *13*, 639−650.
(64) Laufer, J.; Johnson, P.; Zhang, E.; Treeby, B.; Cox, B.; Pedley, B.; Beard, P. *In Vivo* Preclinical Photoacoustic Imaging of Tumor Vasculature Development and Therapy. *J. Biomed. Opt.* **2012**, *17*, No. 056016.
(65) Levi, J.; Kothapalli, S. R.; Bohndiek, S.; Yoon, J. K.; Dragulescu-Andrasi, A.; Nielsen, C.; Tisma, A.; Bodapati, S.; Gowrishankar, G.; Yan, X.; Chan, C.; Starcevic, D.; Gambhir, S. S. Molecular Photoacoustic Imaging of Follicular Thyroid Carcinoma. *Clin. Cancer Res.* **2013**, *19*, 1494−1502.
(66) Wu, J.; You, L.; Chaudhry, S. T.; He, J.; Cheng, J.-X.; Mei, J. Ambient Oxygen-Doped Conjugated Polymer for pH-Activatable Aggregation-Enhanced Photoacoustic Imaging in the Second Near-Infrared Window. *Anal. Chem.* **2021**, *93*, 3189−3195.
(67) Sun, X.; Xu, L.; Xu, H.-D.; Xie, L.; Wang, R.; Yang, Z.; Zhan, W.; Shen, S.; Liang, G. Intracellular Nitroreductase-Triggered "On" and "Enhanced" Photoacoustic Signals for Sensitive Imaging of Tumor Hypoxia. *Adv. Healthcare Mater.* **2023**, No. 2303472.
(68) Cheng, X.; Sun, R.; Yin, L.; Chai, Z.; Shi, H.; Gao, M. Light-Triggered Assembly of Gold Nanoparticles for Photothermal Therapy and Photoacoustic Imaging of Tumors *In Vivo*. *Adv. Mater.* **2017**, *29*, No. 1604894.
(69) Soenen, S. J.; Manshian, B.; Montenegro, J. M.; Amin, F.; Meermann, B.; Thiron, T.; Cornelissen, M.; Vanhaecke, F.; Doak, S.; Parak, W. J.; De Smedt, S.; Braeckmans, K. Cytotoxic Effects of Gold Nanoparticles: A Multiparametric Study. *ACS Nano* **2012**, *6*, 5767−5783.
(70) Wang, C.; Du, W.; Wu, C.; Dan, S.; Sun, M.; Zhang, T.; Wang, B.; Yuan, Y.; Liang, G. Cathespin B-Initiated Cypate Nanoparticle Formation for Tumor Photoacoustic Imaging. *Angew. Chem., Int. Ed.* **2022**, *61*, No. e202114766.
(71) Wang, Y.; Hu, X.; Weng, J.; Li, J.; Fan, Q.; Zhang, Y.; Ye, D. A Photoacoustic Probe for the Imaging of Tumor Apoptosis by Caspase-Mediated Macrocyclization and Self-Assembly. *Angew. Chem., Int. Ed.* **2019**, *58*, 4886−4890.
(72) Richardson, J. C.; Bowtell, R. W.; Mäder, K.; Melia, C. D. Pharmaceutical Applications of Magnetic Resonance Imaging (MRI). *Adv. Drug Deliver. Rev.* **2005**, *57*, 1191−1209.
(73) Padmanabhan, P.; Kumar, A.; Kumar, S.; Chaudhary, R. K.; Gulyás, B. Nanoparticles in Practice for Molecular-Imaging Applications: An Overview. *Acta Biomaterialia* **2016**, *41*, 1−16.
(74) Yang, J.; Feng, J.; Yang, S.; Xu, Y.; Shen, Z. Exceedingly Small Magnetic Iron Oxide Nanoparticles for T_1-Weighted Magnetic Resonance Imaging and Imaging-Guided Therapy of Tumors. *Small* **2023**, *19*, No. e2302856.
(75) Brito, B.; Price, T. W.; Gallo, J.; Banobre-Lopez, M.; Stasiuk, G. J. Smart Magnetic Resonance Imaging-Based Theranostics for Cancer. *Theranostics* **2021**, *11*, 8706−8737.
(76) Jiang, Q.; Liu, X.; Liang, G.; Sun, X. Self-assembly of Peptide Nanofibers for Imaging Applications. *Nanoscale* **2021**, *13*, 15142−15150.
(77) Tirotta, I.; Dichiarante, V.; Pigliacelli, C.; Cavallo, G.; Terraneo, G.; Bombelli, F. B.; Metrangolo, P.; Resnati, G. ^{19}F Magnetic Resonance Imaging (MRI): from Design of Materials to Clinical Applications. *Chem. Rev.* **2015**, *115*, 1106−1129.
(78) Khairnar, S.; More, N.; Mounika, C.; Kapusetti, G. Advances in Contrast Agents for Contrast-Enhanced Magnetic Resonance Imaging. *J. Med. Imaging Radiat. Sci.* **2019**, *50*, 575−589.
(79) Zhou, Z.; Yang, L.; Gao, J.; Chen, X. Structure-Relaxivity Relationships of Magnetic Nanoparticles for Magnetic Resonance Imaging. *Adv. Mater.* **2019**, *31*, No. e1804567.
(80) Babic, A.; Vorobiev, V.; Trefalt, G.; Crowe, L. A.; Helm, L.; Vallee, J. P.; Allemann, E. MRI Micelles Self-Assembled from Synthetic Gadolinium-Based Nano Building Blocks. *Chem. Commun.* **2019**, *55*, 945−948.
(81) Hua, Y.; Pu, G.; Ou, C.; Zhang, X.; Wang, L.; Sun, J.; Yang, Z.; Chen, M. Gd(III)-Induced Supramolecular Hydrogelation with Enhanced Magnetic Resonance Performance for Enzyme Detection. *Sci. Rep.* **2017**, *7*, 40172.
(82) Xu, H.-D.; Cheng, X.; Sun, X.; Chen, P.; Zhan, W.; Liu, X.; Wang, X.; Hu, B.; Liang, G. Caspase-3-Triggered Intracellular Gadolinium Nanoparticle Formation for T_1-Weighted Magnetic Resonance Imaging of Apoptosis *In Vivo*. *Nano Lett.* **2023**, *23*, 6178−6183.
(83) Ye, D.; Shuhendler, A. J.; Pandit, P.; Brewer, K. D.; Tee, S. S.; Cui, L.; Tikhomirov, G.; Rutt, B.; Rao, J. Caspase-Responsive Smart Gadolinium-Based Contrast Agent for Magnetic Resonance Imaging of Drug-Induced Apoptosis. *Chem. Sci.* **2014**, *5*, 3845−3852.
(84) Zhou, Z.; Zhao, Z.; Zhang, H.; Wang, Z.; Chen, X.; Wang, R.; Chen, Z.; Gao, J. Interplay Between Longitudinal and Transverse Contrasts in Fe_3O_4 Nanoplates with (111) Exposed Surfaces. *ACS Nano* **2014**, *8*, 7976−7985.
(85) Yuan, Y.; Ding, Z.; Qian, J.; Zhang, J.; Xu, J.; Dong, X.; Han, T.; Ge, S.; Luo, Y.; Wang, Y.; Zhong, K.; Liang, G. Casp3/7-Instructed Intracellular Aggregation of Fe_3O_4 Nanoparticles Enhances T_2 MR Imaging of Tumor Apoptosis. *Nano Lett.* **2016**, *16*, 2686−2691.
(86) Wang, Y.; Li, X.; Chen, P.; Dong, Y.; Liang, G.; Yu, Y. Enzyme-Instructed Self-Aggregation of Fe_3O_4 Nanoparticles for Enhanced MRI T_2 Imaging and Photothermal Therapy of Tumors. *Nanoscale* **2020**, *12*, 1886−1893.
(87) Pellico, J.; Gawne, P. J.; de Rosales, R. T. M. Radiolabelling of Nanomaterials for Medical Imaging and Therapy. *Chem. Soc. Rev.* **2021**, *50*, 3355−3423.
(88) Ametamey, S. M.; Honer, M.; Schubiger, P. A. Molecular Imaging with PET. *Chem. Rev.* **2008**, *108*, 1501−1516.

https://doi.org/10.1021/cbmi.3c00117
Chem. Biomed. Imaging 2024, 2, 98−116

(89) Gawne, P. J.; Man, F.; Blower, P. J.; de Rosales, R. T. M. Direct Cell Radiolabeling for *In Vivo* Cell Tracking with PET and SPECT Imaging. *Chem. Rev.* **2022**, *122*, 10266−10318.
(90) Hughes, D. J.; Subesinghe, M.; Taylor, B.; Bille, A.; Spicer, J.; Papa, S.; Goh, V.; Cook, G. J. R. ^{18}F FDG PET/CT and Novel Molecular Imaging for Directing Immunotherapy in Cancer. *Radiology* **2022**, *304*, 246−264.
(91) Qiu, L.; Li, K.; Dong, W.; Seimbille, Y.; Liu, Q.; Gao, F.; Lin, J. Tumor Microenvironment Responsive "Head-to-Foot" Self-Assembly Nanoplatform for Positron Emission Tomography Imaging in Living Subjects. *ACS Nano* **2021**, *15*, 18250−18259.
(92) Lin, J.; Gao, D.; Wang, S.; Lv, G.; Wang, X.; Lu, C.; Peng, Y.; Qiu, L. Stimuli-Responsive Macrocyclization Scaffold Allows *In Situ* Self-Assembly of Radioactive Tracers for Positron Emission Tomography Imaging of Enzyme Activity. *J. Am. Chem. Soc.* **2022**, *144*, 7667−7675.
(93) Shen, B.; Jeon, J.; Palner, M.; Ye, D.; Shuhendler, A.; Chin, F. T.; Rao, J. Positron Emission Tomography Imaging of Drug-Induced Tumor Apoptosis with a Caspase-Triggered Nanoaggregation Probe. *Angew. Chem., Int. Ed.* **2013**, *52*, 10511−10514.
(94) Chen, M.; Chen, Z.; Castillo, J. B.; Cui, L.; Zhou, K.; Shen, B.; Xie, J.; Chin, F. T.; Rao, J. [^{18}F]-C-SNAT4: an Improved Caspase-3-Sensitive Nanoaggregation PET Tracer for Imaging of Tumor Rresponses to Chemo- and Immunotherapies. *Eur. J. Nucl. Med. Mol. Imaging* **2021**, *48*, 3386−3399.
(95) Gambhir, S. S. Molecular Imaging of Cancer with Positron Emission Tomography. *Nat. Rev. Cancer* **2002**, *2*, 683−693.
(96) Wang, H.; Chen, P.; Wu, H.; Zou, P.; Wu, J.; Liu, Y.; Liang, G. Furin-Guided Intracellular ^{68}Ga Nanoparticle Formation Enhancing Tumor MicroPET Imaging. *Anal. Chem.* **2019**, *91*, 14842−14845.
(97) Lee, S. Y.; Jeon, S. I.; Jung, S.; Chung, I. J.; Ahn, C.-H. Targeted Multimodal Imaging Modalities. *Adv. Drug Delivery Rev.* **2014**, *76*, 60−78.
(98) Louie, A. Multimodality Imaging Probes: Design and Challenges. *Chem. Rev.* **2010**, *110*, 3146−3195.
(99) Bai, H.; Wang, Y.; Hu, Y.; Ye, D. A Caspase-3-Activatable Bimodal Probe for Photoacoustic and Magnetic Resonance Imaging of Tumor Apoptosis *In Vivo*. *Biosens. Bioelectron.* **2022**, *216*, No. 114648.
(100) Wang, Y.; Bai, H.; Miao, Y.; Weng, J.; Huang, Z.; Fu, J.; Zhang, Y.; Lin, J.; Ye, D. Tailoring a Near-Infrared Macrocyclization Scaffold Allows the Control of *In Situ* Self-Assembly for Photoacoustic/PET Bimodal Imaging. *Angew. Chem., Int. Ed.* **2022**, *61*, No. e202200369.
(101) Fu, Q.; Feng, H.; Su, L.; Zhang, X.; Liu, L.; Fu, F.; Yang, H.; Song, J. An Activatable Hybrid Organic-Inorganic Nanocomposite as Early Evaluation System of Therapy Effect. *Angew. Chem., Int. Ed.* **2022**, *61*, No. e202112237.

https://doi.org/10.1021/cbmi.3c00117
Chem. Biomed. Imaging 2024, 2, 98−116